ISSN 1063-7729, Astronomy Reports, 2015, Vol. 59, No. 4, pp. 288–312. © Pleiades Publishing, Ltd., 2015.
Original Russian Text © T.S. Khruzina, P.Yu. Golysheva, N.A. Katysheva, S.Yu. Shugarov, N.I. Shakura, 2015, published in Astronomicheskii Zhurnal, 2015, Vol. 92, No. 4, pp. 323–349.

The Dwarf Nova V1239 Herculis in Quiescence

T. S. Khruzina[1*], P. Yu. Golysheva[1], N. A. Katysheva[1], S. Yu. Shugarov[1,2], and N. I. Shakura[1]

[1] *Sternberg Astronomical Institute, Moscow State University, Universitetskii pr. 13, Moscow 119991, Russia*

[2] *Astronomical Institute of the Slovak Academy of Sciences, Tatranska Lomnica, Slovakia*

Received October 21, 2014; in final form, November 21, 2014

Abstract—The results of a study of the integrated brightness of the SU UMa eclipsing binary V1239 Her are presented. The system was monitored on nine nights in 2013–2014 when the binary was in quiescence. The orbital period is refined ($P_{\rm orb} = 0.100082222(2)^{\rm d}$) and the system's light curves obtained. These curves provide evidence for active processes in the system between outbursts: the depths of both minima and the amplitude of the pre-eclipse hump vary, and one of the light curves exhibits no hump at all. The parameters of the accretion disk, hot spot, and gas stream in V1239 Her for several epochs are determined in a "combined" model taking into account the contributions to the total radiation flux from the opaque part of the gas stream and the hot spot on the lateral surface of the disk. Lower limits for the time scale for variations of the disk characteristics are estimated: the viscosity parameter (α_g), temperature of the inner parts of the disk ($T_{\rm in}$), and thickness of the outer edge of the disk (β_d). These can vary appreciably over less than 10 orbital cycles. In the model used, the solution for the light curve that lacks a pre-eclipse hump (JD 2456746) implies the absence of a hot spot on the disk's lateral surface: the radius of the spot is negligible, and temperatures of the spot and at the base of the gas stream are lower than those obtained for the other light curves. The disappearance of the hot spot is accompanied by an abrupt decrease in the disk radius and α_g, as well as a decrease in the thickness of the disk's outer edge. A comparison with the system's parameters derived from the light curve for the previous observation date (JD 2456718) suggests that the disk mass decreased significantly between these two dates ($\sim 280 P_{\rm orb}$); this decrease could be due to a reduced outflow rate from the secondary, as well as the possible infall of a considerable fraction of the matter from the disk onto the surface of the white dwarf.

DOI: 10.1134/S1063772915040034

1. INTRODUCTION

Cataclysmic variables (CVs) are close binary systems with a late-type main-sequence star that fills its Roche lobe and is losing matter that accretes onto its white dwarf (WD) companion through the inner Lagrange point. CVs are subdivided into the two broad subclasses of dwarf novae and nova-like stars, as well as several smaller subclasses (see, for example, the catalog of highly evolved close binaries [1]). Ordinary dwarf novae flare by 2^m–6^m in outbursts that last several days and recur with intervals from several weeks to several months, or even years. Dwarf novae can be subdivided into several subtypes according to the outburst parameters, one of which is SU UMa stars. These systems display two kinds of outbursts: normal outbursts and superoutbursts, which differ from ordinary outbursts in their longer durations and the presence of so-called superhumps in their light curves, whose periods exceed the orbital period by 3–6%. On average, SU UMa stars have the shortest orbital periods among CVs (<3 hours). The shortest orbital periods in this subgroup are possessed by TU Men ($P_{\rm orb} = 2$ hours 81 minutes) and UZ Boo ($P_{\rm orb} \sim 3$ hours).

The very uneven distribution of orbital periods displayed by CVs has been considered in many studies (see, for example, the review in [2]). The main feature of this distribution is the very low number of systems with orbital periods between two and three hours. This interval was called the "period gap," because it was completely void of CVs when these systems were first studied. Proposed explanations of this phenomenon include (1) an abrupt decrease in angular momentum; (2) dynamic instability of the system; and (3) a decrease of the secondary's magnetic activity at the stage when the star becomes completely convective, so that mass transfer via the inner Lagrange point is temporarily discontinued. In the "standard" evolutionary scenario, CVs at early stages of their evolution typically have periods from three to eight hours, with three hours being the upper limit of the period gap, and mass-transfer rates

*E-mail: kts@sai.msu.ru

of 10^{-9}–10^{-8} $M_\odot$/year. A CV loses angular momentum during its evolution, which is taken away by stellar wind from the secondary due to magnetic events. Not long before the end of magnetic braking, the mass transfer abruptly decreases, and the secondary shrinks to the thermal-equilibrium radius, which is inside its Roche lobe. When the orbital period reaches two hours due to the radiation of gravitational waves, mass transfer again begins, at a rate of 10^{-10} $M_\odot$/year. Here, the mass of the secondary can decrease to $\sim$0.05 $M_\odot$.

Further studies gradually filled the period gap. It was first populated with magnetic stars, mainly polars, whose presence in the gap was explained as reflecting the absence of an accretion disk, and thus a different direction of their evolution. With time, the gap became filled with other kinds of CVs as well. Until recently, it contained no SU UMa dwarf novae, with the exception of TU Men, whose period is at the upper limit of the period gap. The first SU UMa system in the middle of the period gap was NY Ser [3]; a detailed review of publications on this system can be found in [4]. By 2003, the gap contained seven SU UMa stars [2], and this number has now increased to about thirty [4–6]. The boundaries adopted for the period gap can differ from study to study: 2–3 hours, or 2.1–2.8 hours. Orbital periods for 26 dwarf novae, 23 of which are SU UMa stars, are presented in [4], where the period gap is somewhat shifted towards longer orbital periods (2.15–3.18 hours).

Studies of the behavior of stars in the period gap are very important, since, from theoretical considerations, a binary in this period range should have no mass transfer from its secondary. However, the presence of SU UMa stars with regular outbursts in the period gap testifies to the existence of mass transfer and must be explained. One of the close binaries in the period gap is the eclipsing system V1239 Her = SDSS J170213.26 + 322954.1, which is the subject of our current study.

Section 2 presents basic information about the parameters of V1239 Her derived earlier from spectroscopic and photometric observations. Section 3 describes our own observations. Sections 4 and 5 consider the ephemeris of V1239 Her and our light curves. Section 6 brief describes the "combined" CV model we used to determine the system's parameters. Section 7 presents the parameters derived from the model light curves of V1239 Her, which we discuss in Section 8. Our main conclusions are summarized in Section 9.

2. MAIN INFORMATION ABOUT THE SYSTEM

V1239 Her = SDSS J170213.26 + 322954.1 was identified as a new eclipsing cataclysmic variable during the Sloan Digital Sky Survey (SDSS) [7].

The first outburst of the system was detected in late September and early October 2005. Boyd et al. [8] present the evolution of white-light light curves as the outburst developed; they found the times of minima and derived the following ephemeris of the orbital variations:

$$\text{Min. phot.} = \text{HJD } 2453648.236507(29) + 0.10008215(1)^{\text{d}}\,E.$$

They also demonstrated that the structure of the light curves between eclipses was very complex, probably due to interference between the orbital and superhump periods. A search for other brightness modulations after subtracting eclipses from the whole set of observations led to the detection of a signal with a period of 0.10496(15) days, which could be the superhump period; the system was classified as an SU UMa star.

The light curve of V1239 Her in quiescence is quite interesting. It has a deep (to $\sim 1.5^m$) minimum ($\varphi \sim 0.0$) corresponding to the primary eclipse with the 2.4-hour period, a secondary minimum with a depth to 0.2^m at phase 0.5, and a large hump (to $\sim 0.2^m$) before the eclipse, due to the appearance of a hot spot in the line of sight. Radial-velocity curves for the Hα and Hβ lines, which have semi-amplitudes of 110 ± 10 and 124 ± 13 km/s, are presented in [7]; the spectral type of the red dwarf was determined as M1.5 ± 1.1, and the distance to the object ($d \simeq 460$–650 pc) was estimated from empirical relations.

Littlefair et al. [9] performed time-resolved ($\sim$2 s) photometry of V1239 Her with the ULTRACAM instrument on the 4.2-m WHT telescope, focusing especially on the eclipse profiles. The data from [9] were re-analyzed in [10]. Considerable flickering was detected near the eclipse ingress ($\varphi > 0.8$), probably originating in the inner disk and hot spot.

Photometry of the star was acquired between August 11 and 25, 2005, when the system was in quiescence [9]. The fluxes from V1239 Her in the u, g, r filters (with effective wavelengths $\lambda\lambda$ 3551, 4686, and 6166 Å) were $u = 18.52^m$, $g = 17.92^m$, and $r = 17.82^m$. The following ephemeris of the system was derived from an analysis of six times of minima:

$$\text{Min. phot.} = \text{HJD } 2453594.39209(4) + 0.10008209(9)^{\text{d}}\,E. \quad (1)$$

The eclipsing character of the variations of V1239 Her and the availability of observations with very high time resolution made it possible to determine the system's basic parameters (see [9, 10] for details) from the shape and duration of the WD's eclipse, under the assumption that the secondary component completely filled its Roche lobe, i.e. $\mu =$

Table 1. Parameters of V1239 Her from [9, 10]

Parameter	Value	Parameter	Value
i, deg	82.55 ± 0.17	K_{wd}, km/s	94.0 ± 2.2
$q = M_{wd}/M_{\rm red}$	4.03 ± 0.08	$K_{\rm red}$, km/s	380 ± 4
M_{wd}, $M_\odot$	0.91 ± 0.03	R_d, a_0	0.290 ± 0.001
$M_{\rm red}$, $M_\odot$	0.223 ± 0.010	T_{wd}, K	15200 ± 1200
R_{wd}, $R_\odot$	0.0092 ± 0.0004	$T_{\rm red}$, K	3800 ± 100 (M0±0.5 V)
R_{wd}, a_0	0.00974 ± 0.00054	d, pc	270 ± 16
$R_{\rm red}$, $R_\odot$	0.252 ± 0.004	$P_{\rm orb}$, min	144.11821(13)
a_0, $R_\odot$	0.945 ± 0.012		

Here a_0 is the distance between the centers of mass of the binary components; K_{wd} and $K_{\rm red}$ are the radial velocity semi-amplitudes of the WD and secondary; d is the distance to the system.

1, where μ is the degree of filling of the secondary's Roche lobe. In this case, the duration of the WD's eclipse depends only on the orbital inclination i and the mass ratio $q = M_{wd}/M_{\rm red}$. Littlefair et al. [9] applied the Nelder–Mead method (the AMOEBA algorithm [11]) to determine unknown parameters of the close binary in the classical model of a CV. The component masses were estimated assuming that the mass of the WD agreed with the theoretical mass–radius relation for a WD with the corresponding effective temperature. The object's effective temperature and distance were estimated from spectroscopy of the red star; the distance to the object was found to be lower than in [7], $d \sim 250$–290 pc. The secondary's mass was also found to be lower than expected for the orbital period and its temperature, and higher than for stars of its mass. Littlefair et al. [9] and Savoury et al. [10] suggested that these findings indicate that the secondary is a highly evolved star: its mass and effective temperature correspond to a star with a strongly decreased fraction of hydrogen. Note also that the mass of the WD, $M_{wd} = (0.91 \pm 0.03)\ M_\odot$, is above the mean mass of WDs in CVs, $\langle M \rangle = (0.76 \pm 0.19)\ M_\odot$. The parameters of V1239 Her derived in [9, 10] are compiled in Table 1.

Data of the American Association of Variable Star Observers (AAVSO, `www.aavso.org`) obtained in white light during a superoutburst in 2005 (eight nights between October 4 and 12) also demonstrate considerable variations in the shape of the V1239 Her light curve. As an example, Fig. 1 shows the system's light curves for October 4 and 11, 2005 (JD 2453648 and 2453655). It is obvious that the light-curve shape changed within several days. While a large hump was observed at phase 0.4–0.5 on October 4, 2005 (JD 2453648), without the pre-eclipse "hump" typical of dwarf novae, we observe a virtually flat out-of eclipse light curve on October 11 (JD 2453655), when the mean brightness decreased by $\sim 1^m$. Here, the depth of the eclipse exceeds 2^m. As was demonstrated in [8], the residual curve after subtracting the orbital light curve clearly reveals superhumps. An estimate of the superhump period gives $P_{sh} = 0.10496(15)^{\rm d}$.

Kato et al. [12, 13] analyzed the behavior of the superhump period and the derivative $P_{\rm dot} = (dP/dt)/P$ for a large number of SU UMa and WZ Sge stars, including V1239 Her during its superoutbursts of 2005 and 2011. They used data by different authors to refine the orbital period ($0.100082207^{\rm d}$), estimated the period excess $\epsilon = (P_{sh} - P_{\rm orb})/P_{\rm orb} = 6.0\%$, where $P_{\rm orb}$ and P_{sh} are the orbital and superhump periods, and confirmed the star's classification as an SU UMa dwarf nova. A list of all known outbursts of V1239 Her is presented in [13]: superoutbursts were observed in September–October 2005, September 2007, October 2009, and July 2011, and ordinary outbursts in July 2006 and February 2009.

3. OBSERVATIONS

Our observations of V1239 Her began in 2004 and continued until July 2014. Since the star's apparent brightness in quiescence is fairly low ($\sim 19^m$), the quality of our V and R data did not enable their use for the analysis. This paper presents the results of our analysis for data from nine nights in 2013–2014 obtained without a filter (in white, or integrated, light) during the system's quiescence. We observed the object with the 1.25-m telescope of Moscow State University's Crimean Station using a VersArray 1340 CCD, with the 60-cm Zeiss-600 telescope of the Astronomical Institute of the Slovak Academy of Sciences (Tatranska Lomnica, Slovak

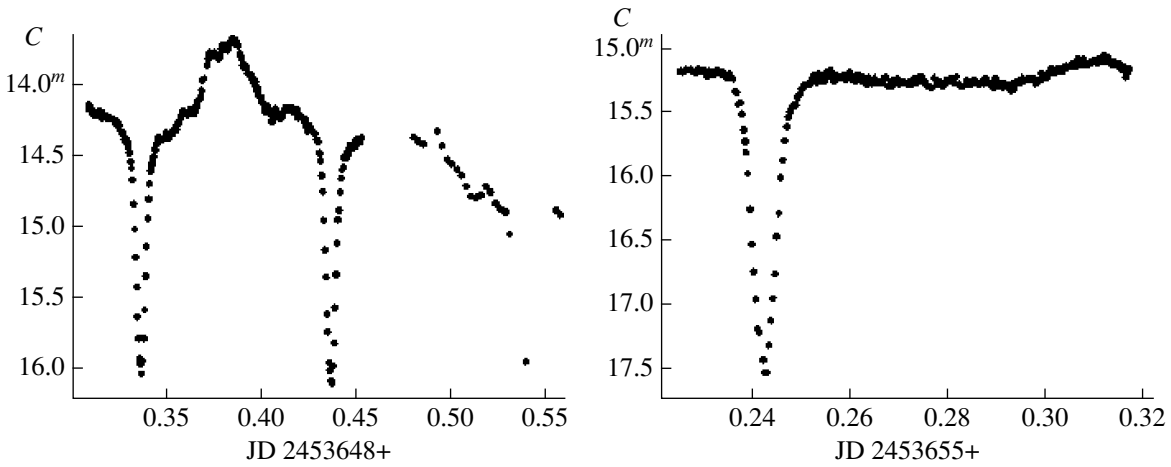

Fig. 1. Light curves of V1239 Her during its outburst in October, 2005 according to AAVSO data.

Republic) using a FLI ML 3041 CCD, and with the Zeiss-1000 telescope of the Special Astrophysical Observatoty (SAO, Russian Academy of Sciences) using a E2V 4000 × 2000 CCD camera. The duration of the observing sessions depended on the weather conditions, and were, on average, two to three hours; the best time resolution was 33 s for the minimum brightness of the orbital light curve and 17 s for the maximum brightness. Table 2 presents a log of our observations.

Since the object is faint, we observed in white, integrated light. We call refer to these broadband observations here as "C". The central wavelength was $\lambda = 6300$ Å and the bandwidth (at the ∼0.5max level) was $\Delta\lambda_{0.5} \sim 4300{-}8300$ Å. The transmission curve was smooth and approximately bell-shaped.

The very nearby star USNO-A2.0 1200-08161936 ("r1", $\alpha(2000) = 17:02:14.250$, $\delta(2000) = +32:29:06.91$) was used as a comparison star; the constancy of its brightness was monitored using several check stars. Since we have not yet performed an accurate brightness determination for this star, we express our measured C magnitudes for the variable in relative, rather than absolute, magnitudes using the relation $\Delta C = 5 + C(\text{V } 1239) - C(\text{r1})$, where "5" is the tentative C magnitude of the comparison star. We reduced the data obtained using the aperture photometry technique in the MAXIM-DL software package.

Figure 2 shows light curves of V1239 Her for the nights listed in Table 2 in relative units: the magnitude differences ΔC between the target and the comparison star are plotted along the vertical axis. This figure shows the variations of the light-curve shape between outbursts. The light curves are arranged in pairs: in the left plots, fractions of the corresponding Julian day are plotted along the horizontal axis; in the right plots, we present phased curves, showing the data folded with the period 0.100082222^{d}. Though the system was in quiescence, the orbital light curve varies, and the orbital pre-eclipse hump is missing on some nights. Brightness variations of this kind were reported in [8]: the light curve changed significantly from cycle to cycle on August 3, 2013 (JD 2456508), when the system was in quiescence.

4. ORBITAL EPHEMERIS

We used code kindly provided by V.P. Goranskij to determine the system's orbital period based on our entire set of data. The power spectrum derived using the Lafler–Kinman method, shown in Fig. 3, clearly reveals a peak corresponding to the orbital period: $P_{\text{orb}} = 0.100082222^{\text{d}}$.

We used the times of minima from [8, 9, 13], the AAVSO data, and our own data (in particular, our observations in Summer 2014) to derive an ephemeris of the orbital variations at our observing epoch. We used all the available data to plot the time dependence of the difference between the observed times of minima and those calculated using the ephemeris, $O{-}C$ (Fig. 4).

Our observations are plotted as filled circles, and data from the literature and the AAVSO as asterisks. There were no visible changes in the orbital period during 10 years. On average, the times of minima deviate from the ephemeris by no more than 30 s, with deviations probably due to uncertainties and ambiguities in the mid-eclipse times for the eclipses of the WD (see below). When plotting the $O{-}C$ diagram, we also used the times of five more recent minima from data we obtained in July, 2014 with the same

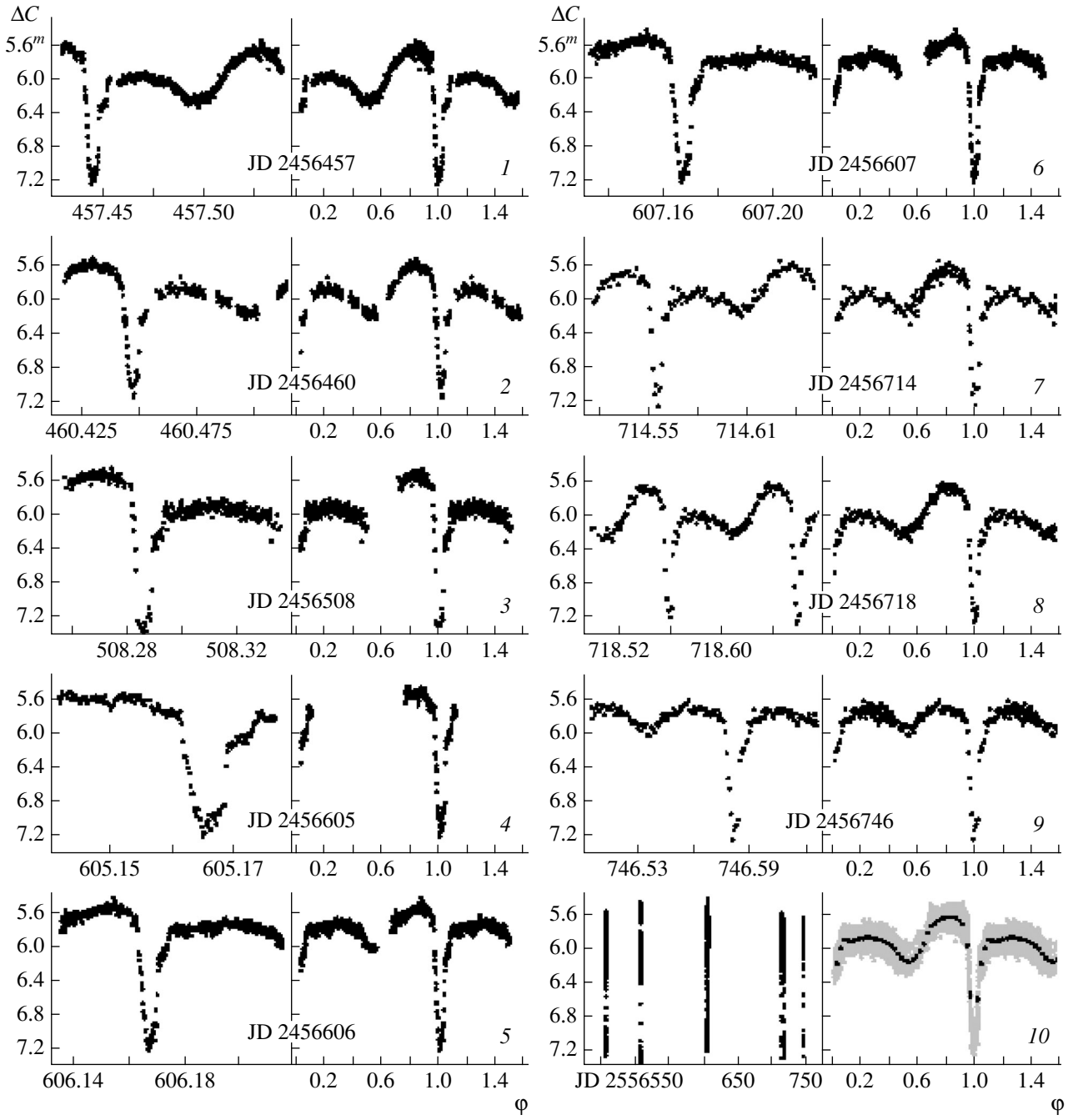

Fig. 2. Panels *1*–*9*: quiescence light curves of V1239 Her observed in 2013–2014 on the dates listed in Table 2. The left panel of each light curve shows the brightness variation with time and the right panel the phased light curve folded with the orbital period $P_{\rm orb} = 0.100082222^{\rm d}$. Panel *10* presents the combined light curve for our observing epoch (left) and the observed and mean phased light curve (grey and black dots, right).

ZTE telescope (see the note to Table 2). We derived the following ephemeris from the $O-C$ diagram, which satisfies all the eclipse times we obtained:

$$\text{Min. phot.} = \text{HJD } 2456508.28346(15) + 0.100082222(2)^{\rm d}\,E. \quad (2)$$

Accurate determination of the time of the minimum corresponding to the mid-eclipse of the WD by the secondary requires observations with high time resolution. Details of the light curve can then be used to find the times of the eclipse ingress and egress for the WD, hot spot, and accretion disk, and thus determine the time of the WD mid-eclipse with good accuracy. More information about this procedure is

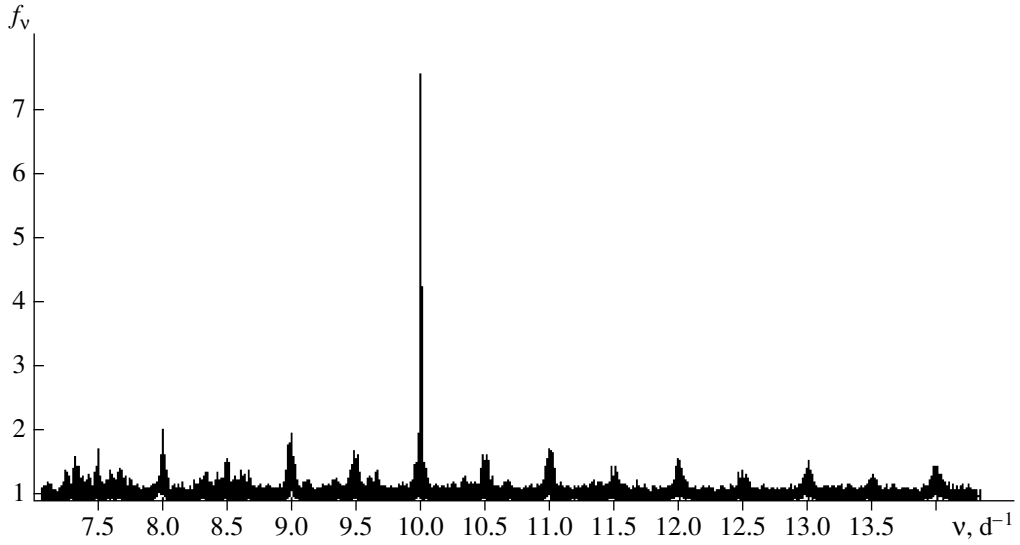

Fig. 3. Power spectrum of V1239 Her derived from our observations using the Lafler–Kinman method.

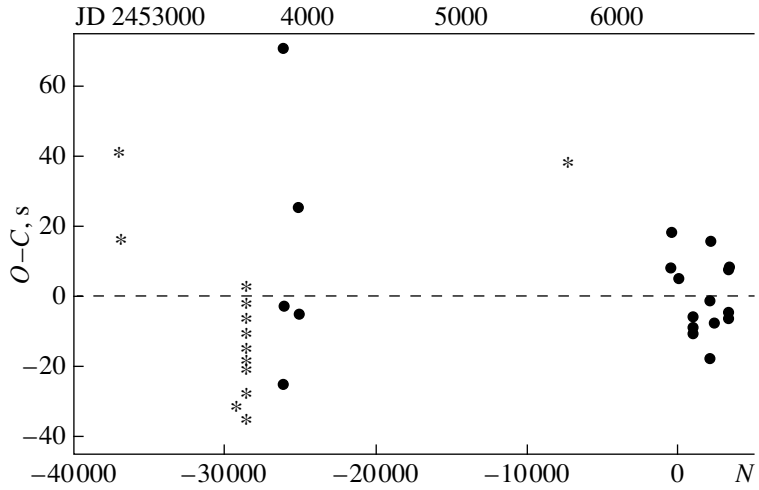

Fig. 4. $O-C$ residuals versus the orbital cycle number N. Filled circles are our observations and asterisks data from the literature or the AAVSO database.

given in [14, 15]. Determination of the middle of the WD eclipse is much more difficult using observations with low time resolution, since it is not possible to reliably fix the times of the eclipse ingress and egress, and the observed brightness minimum does not necessarily correspond to the mid-eclipse of the WD (see [16] for details).

We therefore used the following algorithm to compute the phases of the light curves.

1. We used the ephemeris (2) to compute the orbital phases for the observations obtained in 2013–2014 and plotted the mean light curves.

2. When deriving the close-binary parameters from the observed light-curve shape, we added the orbital-phase shift of the observed light curve relative to the synthetic curve $\Delta\varphi$ to the set of unknown parameters, so that the true WD mid-eclipse time should correspond to phase $\varphi = 0.0$.

3. The computed corrections were added to the phases of the normal points of the mean light curves (Table 3). Table 2 contains the derived times of the WD mid-eclipse, T_n.

5. LIGHT CURVES

The light curves displayed in Fig. 2 can be divided into several groups that are close in time (Fig. 5). We grouped the data (grey points) as follows and plotted the corresponding light curves in Fig. 5. *1*: data of JD 2456457, 460; *2*: JD 2456605, 606, 607; *3*:

Table 2. Log of observations of V1239 Her in 2013–2014

Date	T_1, T_2, JD 2456000+	φ_1, φ_2 (according to (2))	T_n, HJD 2456000+	N	$\Delta C_{\max}$	$\Delta C_{\min}$	Instrument
2013.06.13	457.42926–457.53909	0.853–1.501	457.44386	550	5.535^m	7.232^m	*1*
2013.06.16	460.41709–460.51451	0.699–1.673	460.44693	319	5.539	7.149	*1*
2013.08.03	508.25751–508.33603	0.714–1.499	508.28572	364	5.428	7.347	*2*
2013.11.08	605.14102–605.17672	0.752–1.108	605.16561	199	5.477	7.187	*1*
2013.11.09	606.13527–606.21994	0.684–1.530	606.16617	450	5.377	7.103	*1*
2013.11.10	607.13374–607.21576	0.665–1.485	607.16713	423	5.402	7.189	*1*
2014.02.25	714.51062–714.65289	0.546–1.968	714.55536	161	5.582	7.264	*3*
2014.03.01	718.49238–718.67645	0.339–2.178	718.65818	192	5.622	7.258	*3*
2014.03.29	746.50400–746.62635	0.232–1.455	746.58155	170	5.606	7.237	*3*

T_1, T_2 are the times of the beginning and end of our observations; φ_1, φ_2 the beginning and end phases of the observations, according to (2); T_n the observed time of minimum; N the number of CCD images acquired during the night; and $\Delta C_{\max}$ and $\Delta C_{\min}$ the maximum and minimum magnitudes in a given set of observations. The instruments are: (*1*) the ZTE telescope (Nauchnyi, Crimea) with a VersArray1300 CCD camera, (*2*) the Zeiss-1000 telescope (SAO) with a E2V 4000 × 2000 CCD camera, and (*3*) the Zeiss-600 telescope (Tatranska Lomnica, Slovakia) with a FLI ML 3041 CCD camera.

JD 2456714, 718, and *4*: JD 2456746. We calculated the mean light curve for each group (black dots). Panel *10* (right side) in Fig. 2 and Fig. 5 show that the scatter of the data is considerable, even within two to three nights; this is clearly seen in panel *2* of Fig. 5. The mean light-curve shape also varies. For example, the light curve for March 29 (JD 2456746) lacks an orbital hump (panel *9* in Fig. 2 and panel *4* in Fig. 5), and the fluxes at the eclipse ingress and egress are comparable. Note that the secondary minimum has moved from phase $\varphi \sim 0.5$ to phase $\varphi \sim 0.55$. Such light curve variations make it necessary to analyze each of the available curves in order to determine which parameter variations cause these effects.

Determining the component parameters from photometric data requires reliable light curves that have been cleaned of random flux fluctuations. Our data cover three groups of 2013–2014 observations separated into least 1000 orbital cycles (Fig. 4, Table 2). The system did not experience any outburst activity on the studied dates, but the light-curve shape obviously varied. The mean light curves used to determine the parameters of V1239 Her are presented in Table 3. As a rule, we did not average data within the primary minimum, to avoid distortion of the shape of the minimum. We estimated the uncertainties of such data points using the mean σ value calculated from the corresponding light curve outside the eclipse. The the total number of measurements in a dataset is presented in braces.

6. MODEL OF THE CLOSE BINARY USED TO DETERMINE THE SYSTEM PARAMETERS

Gas-dynamical studies of the steady-state matter flow patterns in close binary systems show that the interaction between the flow and disk is *collisionless* [17–22]. A shock appears, but only in a narrow region along the flow edge (a "hot line"), as a result of the interaction of incoming streams of the disk and circumdisk halo with the matter in the flow. Re-processing of the energy released forms an extended region of enhanced energy release that coincides with the surface of the optically thick part of the gas flow. Bisikalo et al. [17] gave this model the name "hot line", in spite of the finite (3D) character of the shock's extended region, in order to emphasize the difference of the energy release in this model and its location from the case of a conventional "hot spot" model assuming a *collisional* impact of the gas flow with the lateral surface of the accretion disk. In the software developed based on these gas-dynamical computations, the optically thick part of the extended region of enhanced energy release was approximated using a truncated ellipsoid, whose major axis coincides with the axis of the gas flow. We will call the resulting object a hot line (following [17–22]), or alternatively a hot ellipsoid or hot stream, which is more correct from the linguistic point of view. The main morphologic features of the matter flow in a semi-detached binary with a steady-state cool disk ($T_{eff} \sim 10\,000$–$15\,000$ K) are described in [20, 23].

The gas-dynamical computations [20] demonstrate that, in the case of a cool disk, the interaction

Table 3. Mean light curves of V1239 Her obtained in 2013–2014

JD 2456457{65}				JD 2456460{57}				JD 2456508{52}			
φ	ΔC	σ	n	φ	ΔC	σ	n	φ	ΔC	σ	n
0.0040	7.1928	0.0132	6	0.0025	7.0923	0.0384	3	0.0096	7.2943	0.0271	4
0.0154	7.1035	0.0224	6	0.0121	6.9700	0.0180	2	0.0249	7.1423	0.0299	4
0.0250	7.0540	0.0106	4	0.0178	6.8477	0.0071	3	0.0346	6.8580	0.0165	1
0.0327	6.8955	0.0334	4	0.0239	6.8937	0.0045	3	0.0402	6.3080	0.0340	5
0.0442	6.3530	0.0168	8	0.0293	6.6120	0.0126	1	0.0509	6.2693	0.0229	6
0.0586	6.2910	0.0130	7	0.0356	6.2495	0.0191	4	0.0617	6.2092	0.0122	5
0.0721	6.2633	0.0124	7	0.0495	6.2138	0.0118	5	0.0732	6.1380	0.0434	7
0.0957	6.0177	0.0121	11	0.0581	6.1380	0.0126	1	0.0855	5.9328	0.0467	6
0.1462	6.0187	0.0095	12	0.1197	5.9330	0.0156	6	0.0980	5.9531	0.0182	7
0.1692	5.9899	0.0048	12	0.1544	5.9013	0.0221	7	0.1143	5.9517	0.0196	10
0.1912	5.9605	0.0076	11	0.1896	5.9043	0.0146	7	0.1336	5.9130	0.0172	10
0.2113	5.9875	0.0080	10	0.2237	5.8576	0.0179	10	0.1528	5.9441	0.0190	10
0.2305	5.9573	0.0075	10	0.2486	5.8939	0.0047	10	0.1719	5.9352	0.0149	10
0.2496	5.9554	0.0062	10	0.2687	5.9051	0.0089	11	0.1911	5.9100	0.0179	10
0.2688	5.9473	0.0086	10	0.2908	5.9150	0.0088	12	0.2104	5.8888	0.0155	10
0.2879	5.9652	0.0069	10	0.3080	5.9325	0.0179	6	0.2296	5.8905	0.0087	10
0.3071	5.9972	0.0111	10	0.3770	5.9779	0.0117	10	0.2488	5.8731	0.0190	10
0.3262	6.0031	0.0076	10	0.3962	6.0223	0.0104	10	0.2679	5.8856	0.0102	10
0.3454	5.9951	0.0067	10	0.4152	6.0376	0.0093	9	0.2872	5.8606	0.0137	10
0.3645	6.0392	0.0061	10	0.4670	6.1197	0.0081	10	0.3065	5.9006	0.0122	10
0.3837	6.0224	0.0082	10	0.4862	6.1498	0.0119	10	0.3257	5.9170	0.0140	10
0.4028	6.0794	0.0117	10	0.5054	6.1642	0.0101	10	0.3448	5.9167	0.0134	10
0.4220	6.1108	0.0089	10	0.5327	6.1505	0.0142	11	0.3734	5.9461	0.0139	20
0.4412	6.1342	0.0061	10	0.6439	5.9214	0.0139	9	0.4116	5.9696	0.0117	20
0.4603	6.1887	0.0098	10	0.6648	5.8648	0.0151	10	0.4384	5.9594	0.0141	8
0.4795	6.2399	0.0095	10	0.7124	5.7223	0.0147	6	0.4547	5.9860	0.0151	9
0.4987	6.2351	0.0070	10	0.7276	5.6590	0.0122	6	0.4813	6.0518	0.0301	8
0.5187	6.2249	0.0096	10	0.7391	5.6372	0.0074	6	0.7311	5.5857	0.0170	6
0.5388	6.2464	0.0128	10	0.7507	5.6413	0.0092	6	0.7466	5.6162	0.0181	6
0.5580	6.2000	0.0104	10	0.7621	5.6217	0.0097	6	0.7612	5.5538	0.0049	6
0.5771	6.2113	0.0107	10	0.7736	5.6248	0.0126	6	0.7727	5.5417	0.0138	6
0.5963	6.1621	0.0089	10	0.7856	5.6022	0.0167	6	0.7842	5.5312	0.0137	6
0.6154	6.1072	0.0140	10	0.8001	5.5998	0.0090	6	0.7956	5.5342	0.0081	6
0.6346	6.0365	0.0158	10	0.8139	5.5758	0.0097	6	0.8072	5.5160	0.0109	6
0.6537	5.9786	0.0117	10	0.8254	5.5845	0.0177	6	0.8187	5.5260	0.0233	6
0.6729	5.8946	0.0128	10	0.8368	5.5792	0.0090	6	0.8305	5.5090	0.0116	6
0.6920	5.8248	0.0081	10	0.8483	5.6087	0.0044	6	0.8425	5.5155	0.0094	6
0.7112	5.7861	0.0109	10	0.8598	5.6573	0.0070	6	0.8539	5.5190	0.0141	6
0.7303	5.7520	0.0100	10	0.8713	5.6407	0.0111	6	0.8655	5.4877	0.0108	6
0.7495	5.7345	0.0069	10	0.8828	5.6220	0.0097	6	0.8800	5.5216	0.0189	9
0.7687	5.6821	0.0097	10	0.8960	5.6312	0.0159	5	0.8974	5.5336	0.0129	9
0.7878	5.6723	0.0062	10	0.9067	5.6346	0.0047	5	0.9108	5.5490	0.0219	5
0.8070	5.6383	0.0080	10	0.9167	5.6482	0.0119	5	0.9203	5.5604	0.0183	5
0.8261	5.6853	0.0123	10	0.9278	5.7184	0.0121	5	0.9299	5.5936	0.0113	5
0.8453	5.6322	0.0201	10	0.9374	5.7502	0.0131	5	0.9578	5.6290	0.0083	5

Table 3. (Contd.)

JD 2456457{65}				JD 2456460{57}				JD 2456508{52}			
φ	ΔC	σ	n	φ	ΔC	σ	n	φ	ΔC	σ	n
0.8582	5.6440	0.0123	10	0.9460	5.8263	0.0084	4	0.9637	5.8520	0.0165	1
0.8679	5.6431	0.0189	10	0.9537	5.8860	0.0227	4	0.9654	5.9880	0.0165	1
0.8764	5.6466	0.0305	10	0.9584	6.1080	0.0126	1	0.9685	6.1575	0.0166	2
0.8863	5.6591	0.0158	10	0.9661	6.2517	0.0165	7	0.9722	6.0165	0.0075	2
0.8959	5.6728	0.0175	10	0.9738	6.4520	0.0126	1	0.9761	6.3785	0.0166	2
0.9056	5.6825	0.0200	10	0.9758	6.5480	0.0126	1	0.9790	6.6230	0.0165	1
0.9160	5.6990	0.0149	10	0.9776	6.6690	0.0126	1	0.9914	7.2665	0.0226	4
0.9256	5.7457	0.0245	10	0.9796	6.7820	0.0126	1	JD 2456607{59}			
0.9349	5.7385	0.0179	8	0.9834	6.8560	0.0126	1	φ	ΔC	σ	n
0.9456	5.7749	0.0290	9	0.9872	6.9370	0.0126	1	0.0002	7.1345	0.0323	4
0.9580	5.7797	0.0260	8	0.9910	6.9910	0.0126	1	0.0089	7.0690	0.0230	5
0.9686	6.1287	0.0279	3	0.9949	7.0270	0.0126	1	0.0174	6.9332	0.0234	4
0.9742	6.2317	0.0168	3	JD 2456606{54}				0.0232	6.9995	0.0815	2
0.9781	6.4140	0.0136	1	φ	ΔC	σ	n	0.0261	6.7250	0.0165	1
0.9800	6.5400	0.0136	1	0.0021	7.0226	0.0209	9	0.0280	6.8790	0.0165	1
0.9819	6.6670	0.0136	1	0.0138	6.9938	0.0246	4	0.0299	6.9130	0.0165	1
0.9839	6.7650	0.0136	1	0.0210	6.9025	0.0756	4	0.0318	6.5430	0.0165	1
0.9858	6.9320	0.0136	1	0.0291	6.7184	0.0407	5	0.0338	6.2610	0.0165	1
0.9896	7.0550	0.0368	3	0.0346	6.2800	0.0171	1	0.0376	6.1480	0.0168	3
0.9964	7.0807	0.0205	3	0.0444	6.0234	0.0149	10	0.0442	6.1027	0.0325	4
JD 2456605{30}				0.0624	5.9555	0.0182	10	0.0529	6.0660	0.0240	5
φ	ΔC	σ	n	0.0804	5.8479	0.0253	10	0.0605	6.0490	0.0189	3
0.0035	7.0220	0.0371	4	0.0984	5.7300	0.0125	10	0.0672	5.9752	0.0157	4
0.0117	7.0000	0.0341	5	0.1164	5.7609	0.0103	10	0.0720	5.8810	0.0165	1
0.0197	6.9017	0.0127	4	0.1344	5.7711	0.0146	10	0.0826	5.7855	0.0068	10
0.0270	6.8268	0.0128	4	0.1524	5.8031	0.0145	10	0.1017	5.7675	0.0104	10
0.0315	6.3500	0.0177	1	0.1704	5.7754	0.0082	10	0.1209	5.7807	0.0119	10
0.0405	6.1026	0.0151	9	0.1884	5.7912	0.0139	10	0.1400	5.7886	0.0127	10
0.0569	6.0300	0.0115	9	0.2064	5.7625	0.0126	10	0.1592	5.7783	0.0083	10
0.0732	5.9378	0.0287	9	0.2329	5.7964	0.0083	10	0.1783	5.7576	0.0076	10
0.0894	5.7718	0.0142	9	0.2509	5.7249	0.0107	10	0.1975	5.7461	0.0121	10
0.1047	5.7869	0.0068	8	0.2689	5.7598	0.0130	10	0.2167	5.7470	0.0132	10
0.7614	5.5493	0.0167	10	0.2872	5.7553	0.0159	10	0.2358	5.7929	0.0125	10
0.7803	5.5275	0.0111	10	0.3086	5.7504	0.0116	10	0.2550	5.7413	0.0095	10
0.7983	5.5757	0.0084	10	0.3277	5.7714	0.0224	10	0.2741	5.6871	0.0151	10
0.8163	5.5578	0.0069	10	0.3469	5.7586	0.0112	10	0.2933	5.7989	0.0086	10
0.8343	5.5909	0.0106	10	0.3661	5.7710	0.0100	10	0.3124	5.7017	0.0098	10
0.8523	5.5924	0.0189	10	0.3852	5.7802	0.0138	10	0.3316	5.7170	0.0111	10
0.8703	5.5447	0.0098	10	0.4044	5.7950	0.0127	10	0.3507	5.7382	0.0121	10
0.8883	5.5667	0.0123	10	0.4235	5.8532	0.0080	10	0.3699	5.7246	0.0140	10
0.9063	5.6349	0.0185	10	0.4427	5.8537	0.0100	10	0.3890	5.7431	0.0104	10
0.9225	5.6854	0.0119	8	0.4618	5.9177	0.0117	10	0.4082	5.7735	0.0129	10
0.9369	5.7230	0.0109	8	0.4813	5.9534	0.0127	10	0.4264	5.8027	0.0122	9
0.9513	5.7438	0.0097	8	0.5048	5.9373	0.0134	9	0.4436	5.8080	0.0142	9
0.9593	5.8510	0.0177	1	0.5272	5.9711	0.0140	9	0.4608	5.8449	0.0216	9
0.9612	6.0600	0.0177	1	0.6980	5.5472	0.0193	9	0.4781	5.8808	0.0114	9

Table 3. (Contd.)

JD 2456605{30}				JD 2456606{54}				JD 2456607{59}			
φ	ΔC	σ	n	φ	ΔC	σ	n	φ	ΔC	σ	n
0.9657	6.2562	0.0140	4	0.7131	5.5008	0.0154	9	0.6842	5.6762	0.0195	10
0.9711	6.4090	0.0300	2	0.7292	5.5161	0.0145	10	0.7052	5.6270	0.0191	10
0.9756	6.6507	0.0324	3	0.7474	5.5171	0.0131	10	0.7244	5.6474	0.0187	10
0.9828	6.8774	0.0155	5	0.7661	5.4967	0.0076	10	0.7436	5.6113	0.0110	10
0.9900	7.0097	0.0322	3	0.7841	5.4789	0.0085	10	0.7627	5.6222	0.0108	10
0.9963	7.1212	0.0354	4	0.8021	5.4841	0.0097	10	0.7818	5.5866	0.0098	10
JD 2456718{40}				0.8201	5.4613	0.0100	10	0.8010	5.5615	0.0074	10
φ	ΔC	σ	n	0.8381	5.4473	0.0111	10	0.8202	5.5333	0.0074	10
0.0100	7.1790	0.0310	5	0.8561	5.4487	0.0074	10	0.8393	5.5281	0.0104	10
0.0256	7.1645	0.0178	2	0.8750	5.4882	0.0087	10	0.8585	5.5260	0.0104	10
0.0302	7.0770	0.0177	1	0.8932	5.4538	0.0086	10	0.8776	5.5001	0.0186	10
0.0383	6.6650	0.0177	1	0.9113	5.4576	0.0079	10	0.8958	5.5362	0.0134	9
0.0398	6.4540	0.0177	1	0.9292	5.4661	0.0132	10	0.9131	5.5624	0.0042	9
0.0639	6.2792	0.0182	9	0.9463	5.5684	0.0172	9	0.9293	5.5817	0.0084	8
0.0968	6.0925	0.0144	6	0.9580	5.5740	0.0166	4	0.9427	5.6907	0.0163	6
0.1224	6.0150	0.0180	6	0.9625	5.7490	0.0171	1	0.9552	5.6946	0.0246	7
0.1543	6.0297	0.0147	6	0.9661	5.9973	0.0033	3	0.9648	6.0860	0.0254	3
0.1953	5.9922	0.0166	6	0.9697	6.0930	0.0171	1	0.9705	6.2463	0.0224	3
0.2447	6.0202	0.0172	6	0.9724	6.4005	0.0185	2	0.9753	6.4445	0.0315	2
0.2956	6.0388	0.0253	6	0.9769	6.6407	0.0568	3	0.9820	6.7598	0.0327	5
0.3425	6.0228	0.0124	6	0.9823	6.7210	0.0789	3	0.9887	6.9600	0.0070	2
0.3830	6.0710	0.0074	6	0.9895	6.9706	0.0186	5	0.9935	7.1060	0.0164	3
0.4212	6.1202	0.0136	6	JD 2456714{35}				JD 2456746{37}			
0.4612	6.1623	0.0189	6	φ	ΔC	σ	n	φ	ΔC	σ	n
0.4995	6.2202	0.0167	6	0.0065	7.2640	0.0240	1	0.0075	7.0877	0.0197	3
0.5288	6.2077	0.0165	6	0.0203	7.0555	0.0105	2	0.0258	7.0040	0.0188	2
0.5561	6.2063	0.0264	6	0.0342	6.7700	0.0240	1	0.0368	6.3050	0.0186	1
0.5833	6.1427	0.0148	6	0.0570	6.2195	0.0134	4	0.0515	6.1860	0.0133	3
0.6101	6.1018	0.0159	6	0.1028	6.0228	0.0340	6	0.0598	6.0830	0.0150	2
0.6371	6.0675	0.0240	6	0.1578	5.9788	0.0257	6	0.0991	5.8497	0.0358	6
0.6643	5.9683	0.0135	6	0.2081	5.9682	0.0115	5	0.1431	5.8087	0.0200	6
0.6915	5.8740	0.0251	6	0.2538	5.9132	0.0147	5	0.1871	5.7345	0.0133	6
0.7187	5.7890	0.0127	6	0.2996	5.9536	0.0231	5	0.2251	5.7328	0.0169	6
0.7456	5.7587	0.0216	6	0.3453	6.0312	0.0132	5	0.2451	5.6985	0.0266	6
0.7725	5.6768	0.0154	6	0.3909	5.9890	0.0162	5	0.2648	5.7073	0.0174	6
0.7997	5.6812	0.0140	6	0.4339	6.0532	0.0246	5	0.2852	5.7258	0.0195	6
0.8269	5.6870	0.0170	6	0.4767	6.1166	0.0150	5	0.3054	5.7258	0.0200	6
0.8542	5.6962	0.0130	6	0.5197	6.1388	0.0225	5	0.3276	5.7567	0.0355	6
0.8785	5.6746	0.0141	5	0.5597	6.1094	0.0378	7	0.3496	5.7447	0.0346	6
0.9015	5.7282	0.0091	5	0.5871	6.0494	0.0365	7	0.3717	5.7753	0.0200	6
0.9240	5.7494	0.0164	5	0.6218	6.0081	0.0336	8	0.3937	5.7662	0.0242	6
0.9444	5.8403	0.0250	4	0.6576	5.8800	0.0204	8	0.4157	5.8032	0.0220	6
0.9594	5.8847	0.0241	3	0.6864	5.7872	0.0253	5	0.4377	5.8032	0.0232	6
0.9713	6.3240	0.0300	2	0.7086	5.7484	0.0307	5	0.4682	5.8662	0.0129	6
0.9789	6.4900	0.0177	1	0.7310	5.7166	0.0196	5	0.5122	5.9018	0.0118	6
0.9819	6.6300	0.0177	1	0.7572	5.6924	0.0318	7	0.5563	5.9665	0.0184	6

Table 3. (Contd.)

JD 2456718{40}				JD 2456714{35}				JD 2456746{37}			
φ	ΔC	σ	n	φ	ΔC	σ	n	φ	ΔC	σ	n
0.9874	6.8250	0.0177	1	0.7886	5.6774	0.0154	7	0.6003	5.8657	0.0295	6
0.9938	6.9980	0.0290	2	0.8171	5.6413	0.0216	6	0.6443	5.7923	0.0147	6
				0.8416	5.6722	0.0255	5	0.6884	5.7360	0.0117	6
				0.8636	5.6772	0.0221	5	0.7324	5.6628	0.0106	6
				0.8862	5.7262	0.0329	5	0.7764	5.7007	0.0229	6
				0.9077	5.7278	0.0180	5	0.8205	5.6973	0.0055	6
				0.9304	5.7498	0.0286	5	0.8607	5.7426	0.0146	5
				0.9500	5.8298	0.0158	4	0.8974	5.7356	0.0117	5
				0.9607	6.1130	0.0240	1	0.9341	5.8170	0.0153	5
				0.9678	6.3465	0.0285	2	0.9561	5.9650	0.0186	1
				0.9745	6.5190	0.0240	1	0.9634	6.2200	0.0186	1
				0.9791	6.8220	0.0240	1	0.9708	6.5110	0.0186	1
				0.9928	7.0675	0.0515	2	0.9784	6.6360	0.0186	1
								0.9854	6.9360	0.0186	1
								0.9928	7.2370	0.0186	1

displays typical features of an oblique collision of two streams, forming a structure consisting of two shocks separated by a tangential discontinuity. The region of the collisional interaction between the flow and halo has a complex structure. The density of parts of the halo that are far from the disk is low, and the shock due to their interaction with the flow is located along the edge of the flow. The structure is fairly extended, and this component of the region of energy release is similar to the hot stream found earlier in computations for a hot accretion disk; however, in the case of a cool disk, the surface of the hot ellipsoid on its leeward side does not coincide with the tangent to the lateral surface of the disk, and forms an obtuse angle with it. As the halo gas density increases, the shock bends and assumes a position on the lateral surface of the disk, on the leeward side of the flow. At the interaction site, the halo gas and stream gas pass through the shocks corresponding to their flows and become mixed. This matter then moves along the tangential discontinuity between the two shocks, heating the matter on the leeward side of the disk, similar to the classical hot-spot model.

Note, however, that traditional CV models assume that the center of the hot spot is located at the intersection of the ballistic trajectory of the gas flow from the secondary and matter at the lateral surface of the disk. In the model we have used, based on the gas-dynamical computations [20], the region of energy release is more complex. It consists of regions on the surface of the hot ellipsoid located near the disk and a hot region on the lateral surface of the disk, represented by a half-ellipse on the leeward side of the line. The center of the ellipse coincides with the intersection point of the gas flow axis with the disk. This combined model is described in detail in [24].

The abrupt change in the gas parameters after passage through the shocks also leads to a pressure increase in the region between the shocks, forming a pressure gradient perpendicular to the system's orbital plane. As a result, the gas begins to expand away from the orbital plane until the gas-pressure gradient is equal to the gravitation force. This motion of gas, together with the motion along the tangential discontinuity at the outer edge of the disk, gradually increases the thickness of the circumdisk halo (along the z axis perpendicular to the disk plane), with the region of vertical acceleration being mainly limited to the region of interaction between the disk and the stream. For this reason, this model assumes that the thickness of the disk's outer edge is largest in the region of the stream's impact with the disk, and gradually decreases on the leeward side of the stream, to the unperturbed state of the disk edge. The entire region of the disk where the thickness of its outer edge exceeds the thickness of the undisturbed disk corresponds to the region of the hot spot.

The following *main assumptions* were used when constructing the combined model taking into account the structural features of the region of interaction between the gas stream and disk described above.

1. The close binary system consists of a late-type star with a non-spherical shape and a WD. In CV

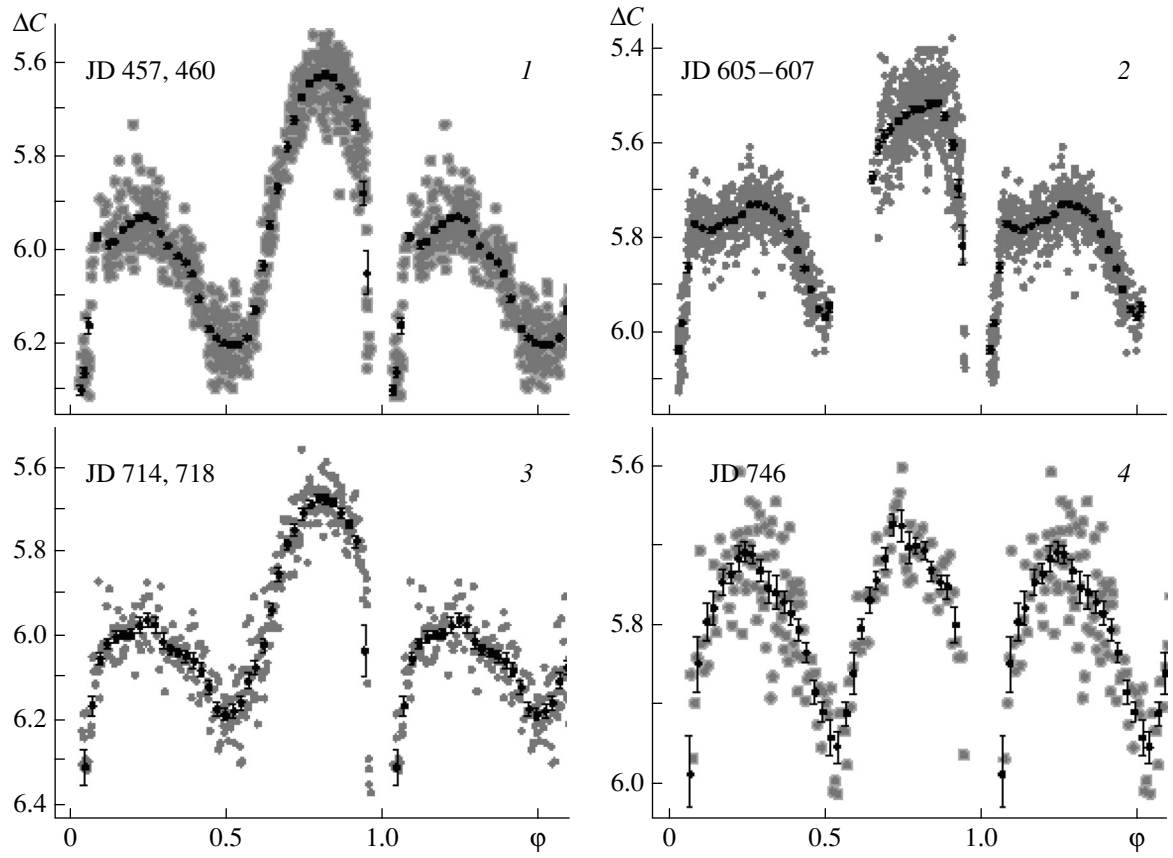

Fig. 5. Phased light curves (grey points) grouped for close dates and mean light curves (black dots) for these data. (*1*) JD 2456457, 460; (*2*) JD 2456605, 606, 607; (*3*) JD 2456714, 718; and (*4*) JD 2456746. The region of the eclipse is not shown.

studies, the WD is traditionally called the primary and the late-type star the secondary. We express all distances in the model in units of the component separation a_0, i.e., $a_0 = 1$. The shape of the secondary (red dwarf) surface is represented by a Roche potential with filling factor $\mu = 1.0$. The stellar surface is subdivided into 648 area elements, for each of which we computed the intensity of the radiation towards the observer, taking into account gravitational darkening and limb darkening (using a non-linear limb-darkening law). The shape of the primary surface is described by a sphere with radius R_{wd}.

2. The primary is surrounded by an optically and geometrically thick elliptical accretion disk (the structure of the disk is described in detail in [25]), with its center located at one of the foci of the disk ellipsoid. The unperturbed disk is represented by the figure formed by the intersection of the *abc* ellipsoid of the disk with semi-axes a, b, and c, and two paraboloids determined by the parameter A_p. The value of A_p changes with the angle ψ of the rotation of the radius vector R_ψ about an axis perpendicular to the orbital plane, according to the expression [25]:

$$A_p(\psi) = \frac{A(1-e^2)}{1+e\cos\psi}, \tag{3}$$

where e is the eccentricity of the disk's *abc* ellipsoid in the orbital plane, $e < 0.1$ and A is a constant (a parameter of the problem). The angle ψ increases clockwise from the periastron point of the disk ellipsoid ($z > 0$ when the system is observed from above). The *abc* ellipsoid determines the shape of the outer (lateral) surface of the disk. The paraboloids give the shape of the inner (upper, $z \geq 0$ and lower, $z < 0$) surfaces of the elliptical accretion disk. The disk orientation is given by the angle α_e between the radius vector from the center of the WD to the periastron point of the disk and the line joining the stellar centers of mass. The disk temperature varies along its radius as

$$T(r) = T_{\rm in}\left(\frac{R_{\rm in}}{r}\right)^{\alpha_g}, \tag{4}$$

where $T_{\rm in}$ is the temperature in the inner regions of the disk, near the stellar equator, at a distance $R_{\rm in} \sim R_{wd}$

from its center. It is usually assumed that, if each point of the disk surface emits like a blackbody, in the first approximation, $\alpha_g = 0.75$ [26]. During a CV's active stage, when the flux from the disk increases by a factor of several hundred, α_g can decrease to $\sim$0.1. As a result, the radial distribution of the temperature becomes flatter and the flux from the accretion disk higher. When computing the local temperature of a given area element on the disk, we took into account heating by radiation from the secondary (this effect is usually insignificant) and high-temperature radiation coming from the inner regions of the disk (this temperature, $T_{\rm in}$, is presumably higher than or equal to the temperature of the WD). This effect also gives rise to a temperature increase of the secondary's surface facing its companion, i.e., the reflection effect.

3. The optically thick part of the gas flow, the hot stream (Fig. 6), is represented by a part of the $a_v b_v c_v$ ellipsoid, whose major axis b_v coincides with the axis of the gas stream flowing from the inner Lagrange point L_1 and whose center is located in the body of the disk, in the orbital plane. It is assumed that $b_v \gg a_v$ and $b_v \gg c_v$; i.e., the ellipsoid describing the shape of the hot stream is quite elongated, with its leeward part forming an obtuse angle with the disk surface. We consider the hot stream to correspond only to the part of this ellipsoid that is outside the accretion disk. The regions of the hot ellipsoid (S_1) closest to the disk have higher temperatures than adjacent parts more distant from the disk, since the collisional interaction between the incoming streams in the disk and the matter of the gaseous stream takes place there.

We assumed that the shock energy is released at the surface of the hot ellipsoid in accordance with a Planck distribution, both at the shock front (i.e., on the side of the incoming flow, or the "windward" side) and at the reverse ("leeward") side. The temperatures of the area elements on the surface of the hot ellipsoid were independently computed for each side. The temperature variations are described with a cosine law, with the maximum values $T_{ww,\max}$ and $T_{lw,\max}$ at the windward and leeward sides. The minimum temperature of the hot ellipsoid at $r_{\min}$ coincides with the temperature of the matter in the absence of heating with shock energy at a distance $r_{\min}$ from the WD center of mass.

4. To model the region of interaction between the disk and the stream (the perturbed disk) on the leeward side, we assumed that a region with a complex shape and with a temperature higher than in adjacent regions — i.e., a hot spot — is located there, on the lateral surface of the disk. The thickness of the outer edge of the disk in the hot-spot region can be either the same as or larger than for the unperturbed disk, where $z = z_{cr}$. Formulas that can be used to determine z_{cr} are presented in [25]. When the thickness of the disk edge exceeds z_{cr}, the disk thickness in the region of the hot spot, c_{sp}, is determined by the parameter k_{sp}, with $c_{sp} = k_{sp} z_{\max}$. Here, $z_{\max}$ is the z coordinate of the intersection of the disk's lateral surface and the hot ellipsoid, which was computed during the determination of the shapes of the disk and hot stream.

The half-ellipse corresponding to the hot spot is largest in the orbital plane. For the hot-spot half-ellipse located on the leeward side of the gas stream, the spot radius in the orbital plane (R_{sp}) is given by the sum of the semi-axis of the part of the hot ellipsoid where it intersects the disk surface (x_{lw}) and the radius of the part of the hot spot that is not covered by the body of the hot ellipsoid, a_{sp}; i.e. $R_{sp} = x_{lw} + a_{sp}$. If we first specify R_{sp} when searching for the parameters of the system components, we can encounter situations when R_{sp} is smaller than x_{lw}, since x_{lw} and R_{sp} are independent and not known in advance. There is no hot spot if $a_{sp} = 0$; i.e. $R_{sp} = x_{sp}$. a_{sp} is a model parameter. There is no hot spot on the windward side of the gas flow.

The local temperature at point j on the disk inside the hot spot increases according to

$$T_j = T_d + T_U \cos\left(\frac{\pi r_j}{2R_{sp}}\right), \qquad (5)$$

where T_U is the temperature of the matter at the point U where the hot stream intersects the disk. T_U is a function of the temperature of the hot ellipsoid near the disk surface on its leeward side, T_{lw}; this is not specified explicitly, thereby reducing the number of unknown parameters. In Eq. (5), r_j is the length of the radius vector from the point U to the center of the area element j. If point j is not in the region of the hot spot, its temperature remains the same (T_d), and is determined only by the distance from the compact object and heating by the radiation of the components.

Thus, formally, the unknown parameters in the model used are the

(1) component-mass ratio $q = M_{wd}/M_{\rm red}$;

(2) orbital inclination, i;

(3, 4) effective temperatures of the WD, T_{wd}, and red donor, $T_{\rm red}$;

(5) radius of the WD, R_{wd};

(6) temperature in the inner regions of the disk (or in the transition layer) near the WD equator, $T_{\rm in}$;

(7–11) parameters of the weakly elliptical disk: its eccentricity e ($e < 0.1$), semi-major axis a, the parameter α_g determining the character of the radial temperature variations in accordance with (4), the periastron azimuth of the disk α_e, the thickness of the disk's outer edge β_d (or the parameter A in (3));

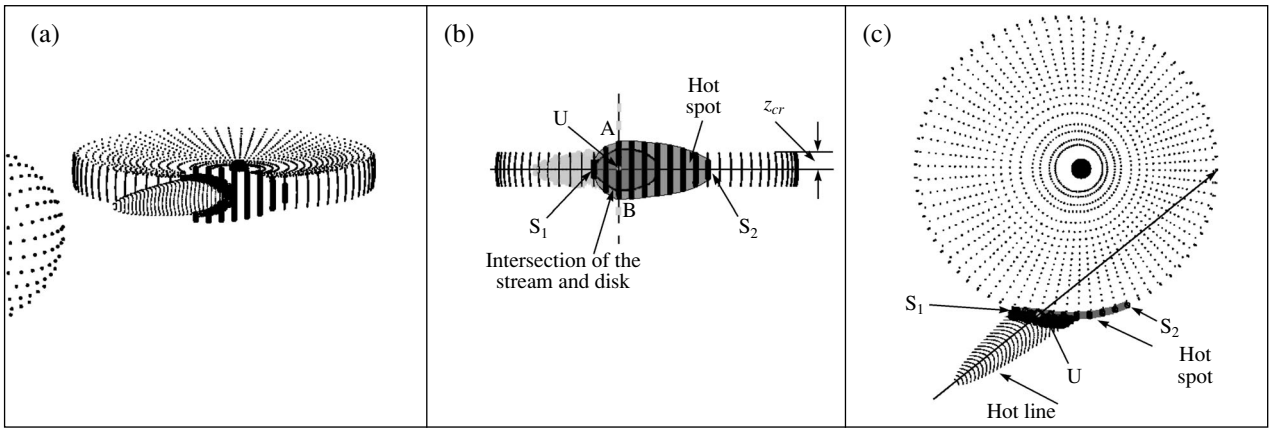

Fig. 6. (a) Schematic representation of the close binary for orbital phase $\varphi = 0.9$ with $q = 9$, $i = 80°$, $R_d = 0.5\xi$, a half-thickness of the outer edge of the unperturbed disk 6.25°, and a half-thickness in the region of the hot spot ∼10°. (b) Schematic representation of the shape of the hot spot on the disk. The orbital inclination is $i = 90°$. The region of the intersection of the hot ellipsoid with the lateral surface of the disk (the oval inside the hot spot) and the region of the hot spot itself are shown; see text for further details. (c) The same system in the plane of the sky.

(12–17) parameters of the hot ellipsoid: the ellipsoid semi-axes a_v, b_v, and c_v; the highest temperatures of the shock-heated matter on the ellipsoid surface near the outer boundary of the disk on the windward, $\Delta T_{ww,\max}$, and leeward, $\Delta T_{lw,\max}$ sides; these temperatures are added to the temperature $T_d(i)$ that matter would have at the given distance from the disk center, $r(i)$, in the absence of the shock, in accordance with the formula $T(i) = T_d(i) + \Delta T_{n,\max} \cos \delta r$, where $n = ww$ or lw and δr is the shift along the axis of the hot stream, which is calculated during the solution of the problem.

The total number of parameters is 17 (the actual number of variables is 22, including the displacement $\Delta\varphi$ described in Section 4, but some of these are technical parameters with very narrow variation ranges; within the establish ranges, the variations of these parameters have little effect on the synthetic light curves, compared to the influence of the main parameters). Thus, we must use additional information about the system to fix some of the parameters and place significant constraints on the variation ranges for the remaining parameters.

We obtained solutions for a set of light curves of V1239 Her obtained using the same comparison star, and mainly differing in the out-of-eclipse flux level. This enabled us to impose additional constraints on the domain of admissible parameter values. Namely, we translated the synthetic light curves for a series of several available light curves into magnitudes using the same unit of energy: the flux from the system at an orbital phase near quadrature, for the light curve with the lowest out-of-eclipse brightness. This approach makes it possible to use both the shape of the synthetic light curves and the flux variations when comparing with the observations. This method has been described in detail in a number of past papers (e.g., [16]).

We solved for the system parameters that provided a synthetic light curve that best matched the observed light curve using the Nelder–Mead method [11], which is also described in [27]. We used several dozen different initial approximations for each light curve when searching for the global minimum of the residuals; since the number of independent variables is large, there are typically a number of local minima in the studied parameter range. We evaluated the agreement between the theoretical and observed light curves in the model considered using residuals calculated as

$$\chi^2 = \sum_{j=1}^{N} \frac{(m_j^{\text{theor}} - m_j^{\text{obs}})^2}{\sigma_j^2}, \qquad (6)$$

where m_j^{theor} and m_j^{obs} are the theoretical and observed magnitudes of the object for the orbital phase j, σ_j^2 is the dispersion of the observations at data point j, and N is the number of normal points in the curve.

7. RESULTS OF MODELING THE V1239 Her LIGHT CURVES

We determined the best-fit system parameters for a series of uniform light curves using the combined model in two stages. In the first, we determined the normalizing flux F_0 needed to translate the theoretical F values into magnitudes and the ΔC_0 value corresponding to this flux. When normalizing a series of uniform light curves, the search for F_0 is usually carried out using only the curve with the lowest out-of-eclipse flux. However, five of the curves for V1239 Her

show no fragments with out-of-eclipse flux, while the out-of-eclipse flux level is approximately the same for the remaining four curves.

For this reason, we first searched for the parameters using each of the four complete light curves independently (JD 2456457, 714, 718, and 746), without reducing them to the same flux level. The parameters q, i, T_{wd}, and R_{wd} were restricted to the ranges $q = 3.95-5.00$, $i = 82°-83°$, $T_{\rm red} = 3600-4000$ K, $e = 0.001-0.1$, $R_d(\max) = (0.289-0.291)a_0 = (0.439-0.457)\xi$, $R_{wd} = (0.0092-0.0103)a_0 = (0.0140-0.0162)\xi$ (here, ξ is the distance between the WD center of mass and the inner Lagrange point L_1, for the selected range of mass ratios, $\xi/a_0 = 0.6369-0.6586$), and $T_{wd} = 15\,000-17\,000$ K, according to [9, 10] (Table 1).

We selected a flux level satisfying all the curves from the sets of solutions obtained for each of the four complete light curves; namely, we assumed that a flux of $F_0 = 7.7$ relative units corresponded to the relative magnitude $\Delta C_0 = 5.8034^m$. The use of relative units is due to the fact that the Planck function used to compute the flux per unit wavelength interval from the area elements (in our case, in centimeters) is the energy flux passing through a 1 cm^2 area. The distance unit in the code is the component separation a_0, which is not known in advance. In the second stage, we searched for the best-fit parameters of V1239 Her for all nine light curves, taking into account the flux normalization to F_0. To reduce the total number of unknown parameters, we fixed the values $q = 4.027$, $i = 82.64°$, $T_{\rm red} = 3730$ K, $R_{wd} = 0.0152\xi$, and $T_{wd} = 15\,660$ K, which are close to the average values presented in Table 1.

The parameters we obtained for V1239 Her from our solutions for each of the nine curves are collected in Table 4. This table also presents some helpful quantities computed for these parameters during the solution. We estimated the uncertainties of the parameters as follows.

Since the uncertainties in the mean points are very small, we were not able to obtain residuals below the critical significance level $\chi^2_{0.001,N}$ for any of our light-curve solutions for V1239 Her (the critical significance level for $\alpha = 0.001$ and the number of degrees of freedom, i.e., the number of normal points in the observed light curve, $N = 30-64$, is $\chi^2_{0.001,N} = 59.7-106$ for the various curves). Thus, we can estimate the influence of variations of a parameter on the solution if we specify some conditional residual limit in place of the critical limit; for example, by increasing the obtained minimal residual for the selected light curve by 10%. The resulting uncertainties of the one to two last digits of each parameter are indicated in brackets.

Along with the parameters yielded by the solution, Table 4 contains a number of quantities derived from one or more of the problem parameters, which demonstrate more clearly the system's characteristics. For example, the temperature T_U is a function of the hot-spot size, the disk radius, the temperature of the shock-heated matter on the leeward side of the hot line, etc., while β_d depends on the disk radius and, in a complex way, the parameter A used to determine the thickness of the disk's outer edge, z_{cr}. The uncertainties of these "dependent" characteristics are determined by the uncertainty of the "independent" parameter that has the largest influence on the quantity in question.

Our estimates of the influence of variations of the parameters that were fixed on the solutions obtained gave the following results: $q = 4.027 \pm 0.44$, $\langle R_{\rm red}\rangle = (0.275 \pm 0.008)a_0$, $\xi = (0.639 \pm 0.011)a_0$, $T_{\rm red} = 3730 \pm 50$ K, $T_{wd} = 15\,660 \pm 280$ K, and $R_{wd} = (0.0152 \pm 0.0003)\xi = (0.0097 \pm 0.0004)a_0$. The solution is most sensitive to the orbital inclination, $i = 82.64° \pm 0.17°$.

Figure 7 presents the theoretical light curves plotted for the corresponding parameters. The observed light curves of V1239 Her in quiescence are reproduced quite satisfactorily, enabling us to draw some conclusions about the variations of the disk parameters as the system brightness decreases in the model used. The quality of our fits of the light curves near the primary minimum is displayed in Fig. 8. For each of the observation dates, we present the unaveraged light curves along with the corresponding curves synthesized using the parameters from Table 4. The same curve is shown with higher orbital-phase resolution to the right, in the range $\varphi \sim 0.8-1.2$. Some of the curves show a small step at orbital phases $\varphi \sim 0.05-0.1$, due to the egress of the windward side of the hot ellipsoid from the eclipse, as follows from a consideration of the relative contributions of the components to the combined brightness.

Figure 9 shows the contributions of the system components to the total flux in relative units: the red dwarf (*1*), white dwarf (*2*), disk with the hot spot (*3*), and hot stream (*4*). Table 5 presents the range of variation of the flux from each component, to facilitate comparison of the light curves for different observation dates.

The following conclusions follow from Fig. 9.

1. The flux from the WD (curves *2*) was constant during the time interval analyzed: in the combined model with the radius and temperature fixed, the brightness of the star can vary only due to eclipses of part of its surface by the disk edge with its changing thickness.

2. The flux $F_{\rm red}$ from the secondary (curves *1*) remained approximately at the same level. The orbital

Table 4. Parameters of V1239 Her in 2013–2014 obtained using the combined model

Parameter	JD 457	JD 460	JD 508	JD 605	JD 606
$q = M_{wd}/M_{\rm red}$	4.027(fixed)				
i, deg	82.64 (fixed)				
$\langle R_{\rm red}\rangle,\ a_0$	0.275 (fixed)				
$T_{\rm red}$, K	3730 (fixed)				
$\xi,\ a_0$	0.639 (fixed)				
R_{wd}	$0.0152\xi = 0.0097a_0$ (fixed)				
T_{wd}, K	15660 (fixed)				
Accretion disk					
e	0.021(20)	0.024(20)	0.030(12)	0.014(13)	0.019(6)
R_d, ξ	0.490(20)	0.482(11)	0.377(13)	0.472(29)	0.468(7)
a, a_0	0.307(11)	0.301(9)	0.234(8)	0.297(18)	0.293(4)
$0.5\beta_d$, deg	1.4(1)	1.2(1)	3.0(3)	1.0(1)	1.7(1)
α_e, deg	83(63)	94(49)	88(2)	103(45)	100(3)
α_g	0.369(3)	0.268(4)	0.488(6)	0.521(5)	0.3653(4)
$\langle T_{\rm in}\rangle$, K	19540(150)	15675(25)	29755(500)	36810(460)	22785(235)
$\langle T_{\rm out}\rangle$, K	5890(40)	6570(63)	7195(200)	6360(75)	7115(66)
Hot spot					
$R_{sp},\ a_0$	0.209(32)	0.193(50)	0.181(30)	0.146(53)	0.202(21)
T_U, K	9330(10)	8985(10)	15760(10)	8275(8)	12380(12)
$0.5z_{sp}$, deg	2.2(3)	1.7(2)	4.7(4)	1.4(3)	2.2(2)
Hot ellipsoid					
$a_v,\ a_0$	0.024(2)	0.022(2)	0.058(2)	0.017(8)	0.027(2)
$b_v,\ a_0$	0.411(29)	0.420(33)	0.328(22)	0.448(40)	0.222(12)
$c_v,\ a_0$	0.008(4)	0.006(2)	0.012(2)	0.006(1)	0.011(1)
$T_{ww,\max}$, K	16105(1400)	14670(2400)	19775(6300)	13895(4900)	18960(6500)
$T_{lw,\max}$, K	15055(270)	14590(700)	19088(950)	13835(750)	18690(390)
β_1, deg	24.1(1)	23.4(1)	12.7(5)	24(3)	21.1(4)
χ^2	1487	3167	2431	1032	1570

Table 4. (Contd.)

Parameter	JD 607	JD 714	JD 718	JD 746
$q = M_{wd}/M_{\rm red}$	4.027 (fixed)			
i, deg	82.64 (fixed)			
$\langle R_{\rm red}\rangle,\ a_0$	0.275 (fixed)			
$T_{\rm red}$, K	3730 (fixed)			
$\xi,\ a_0$	0.639 (fixed)			
R_{wd}	$0.0152\xi = 0.0097a_0$ (fixed)			
T_{wd}, K	15660 (fixed)			
Accretion disk				
e	0.028(16)	0.030(15)	0.029(19)	0.007(6)
R_d, ξ	0.469(33)	0.488(37)	0.566(48)	0.420(16)
a, a_0	0.291(20)	0.303(23)	0.352(30)	0.267(11)
$0.5\beta_d$, deg	1.8(2)	2.1(1)	2.6(2)	0.9(1)
α_e, deg	94(2)	101(44)	92(2)	94(65)
α_g	0.359(5)	0.471(4)	0.556(4)	0.370(4)
$\langle T_{\rm in}\rangle$, K	22360(295)	26930(250)	32630(340)	23790(275)
$\langle T_{\rm out}\rangle$, K	7180(82)	5590(47)	4755(43)	6995(80)
Hot spot				
$R_{sp},\ a_0$	0.214(55)	0.223(33)	0.219(33)	0.053(45)
T_U, K	12455(8)	6830(4)	7675(5)	4893(2)
$0.5z_{sp}$, deg	2.4(3)	4.2(3)	4.3(5)	1.2(4)
Hot ellipsoid				
$a_v,\ a_0$	0.041(1)	0.049(15)	0.035(17)	0.003(2)
$b_v,\ a_0$	0.241(1)	0.371(20)	0.348(20)	0.551(52)
$c_v,\ a_0$	0.009(1)	0.015(1)	0.018(2)	0.005(1)
$T_{ww,\max}$, K	17755(120)	14070(2500)	14000(3100)	12000(1400)
$T_{lw,\max}$, K	17750(90)	12880(305)	12760(265)	11860(680)
β_1, deg	19(3)	18(2)	26(3)	22(1)
χ^2	3179	357	699	651

R_d/ξ is the disk radius at its apastron in units of the distance ξ between the WD center of mass and the inner Lagrange point L_1; $0.5\beta_d$ is the half thickness at the outer edge of the disk (which depends on the two parameters A and a/a_0, see Item 2 in Section 6); a is the semi-major axis of the elliptical disk in units of a_0; $\langle T_{\rm in}\rangle$ and $\langle T_{\rm out}\rangle$ are the mean temperatures in the inner regions (in the transition layer) and at the outer edge of the disk; R_{sp} is the radius of the hot spot on the lateral surface of the disk, on the leeward side of the stream, in units of a_0; T_U is the temperature at the stream axis approximated using the parameter $T_{lw,\max}$ (computed during the solution); $0.5z_{sp}$ is the half thickness of the hot spot (which depends on the parameter k_{sp} and the $z_{\max}$ value computed during the solution); a_v, b_v, and c_v are the semi-axes of the ellipsoid (in units of a_0) with its center inside the disk, where the part of this ellipsoid that is outside the disk describes the shape of the hot stream (these are presented for evaluating the elongation of the truncated ellipsoid); $T_{ww,\max}$ and $T_{lw,\max}$ are the sums of the parameters $\Delta T_{ww,\max}$ and $\Delta T_{lw,\max}$ and the temperature of the matter at the edge of the disk on the corresponding side of the stream (see parameters 12–17 in Item 4 of Section 6); β_1 is the angle formed by the stream axis with the line joining the centers of mass of binary components.

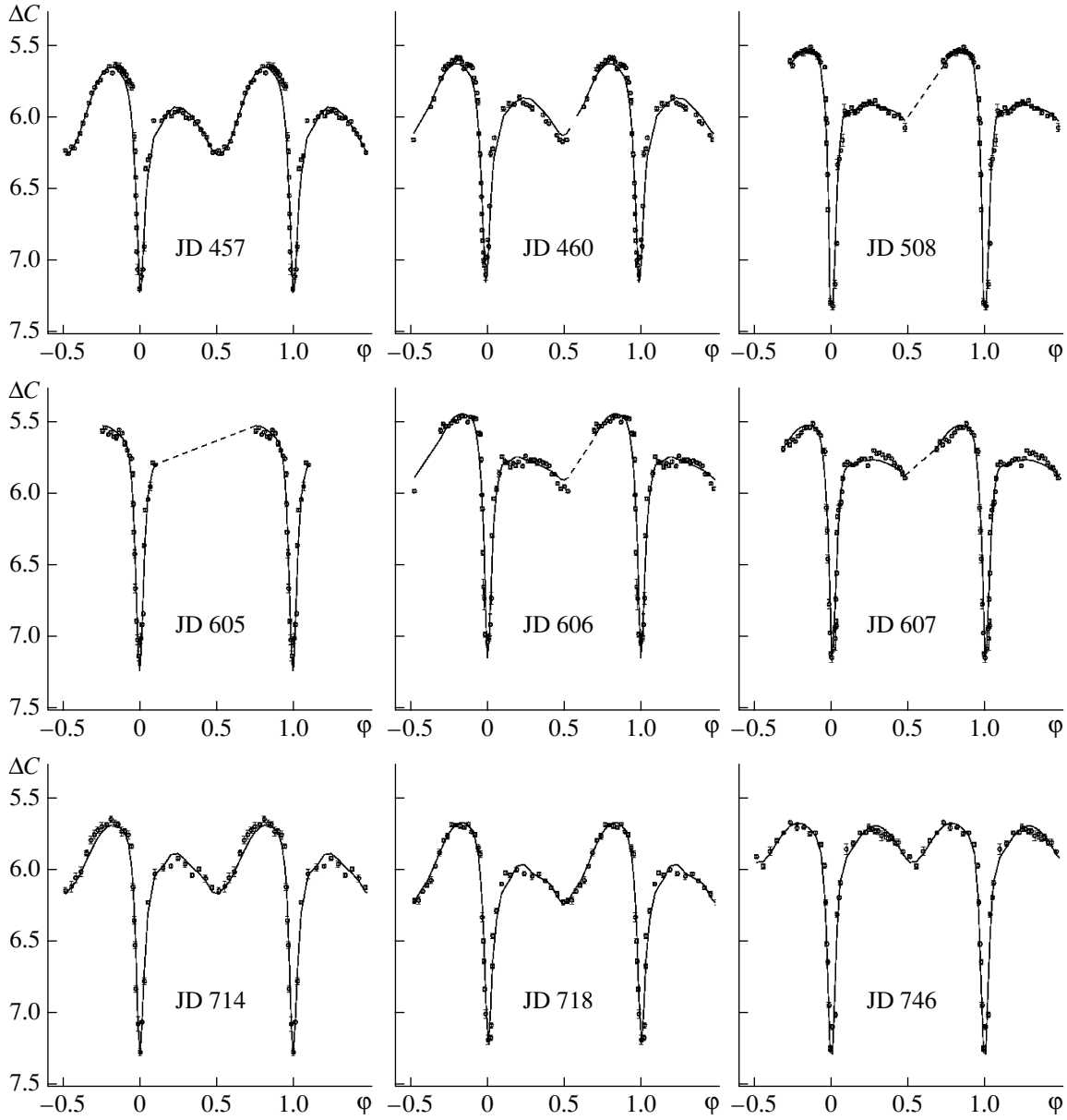

Fig. 7. Mean light curves of V1239 Her (dots) obtained in 2013–2014 together with the synthesized theoretical curves corresponding to the parameters from Table 4 (solid curves). The vertical bars show the rms uncertainties of the points in the mean curves. Each of the panels is labeled with its observation date (the three last digits of the date).

variations of $F_{\rm red}$ of the donor star indicate that ellipsoidal effects are the dominant origin of variability. The role of the reflection effect is not large; it is manifest as a slight increase in the flux at the quadratures and secondary minimum (phases $\varphi \sim 0.5$) in the observations of JD 2456508, 605, and JD 718 (Table 5). In the model used, this is due to the higher temperatures in the inner regions of the disk ($T_{\rm in} >$ 30 000 K).

3. Most important for the formation of the light curve is the flux from the disk and hot spot on its lateral surface (curves *3*). None of the light curves shows a total eclipse of the disk (Table 5). Table 4 shows that the radius of the disk (R_d/a_0) always exceeds the radius of the red dwarf. One exception is the light curve for JD 746, where these radii are the same within the uncertainties. As expected, the flux from the disk at its upper conjunction (phases $\varphi \sim$ 0.3–0.6, approximately coincident with the plateau in the disk light curves), does not show any clear dependence on the disk radius or radial temperature distribution in the disk, α_g.

The orbital hump in the light curves is due to the combined contribution of the hot spot and from light

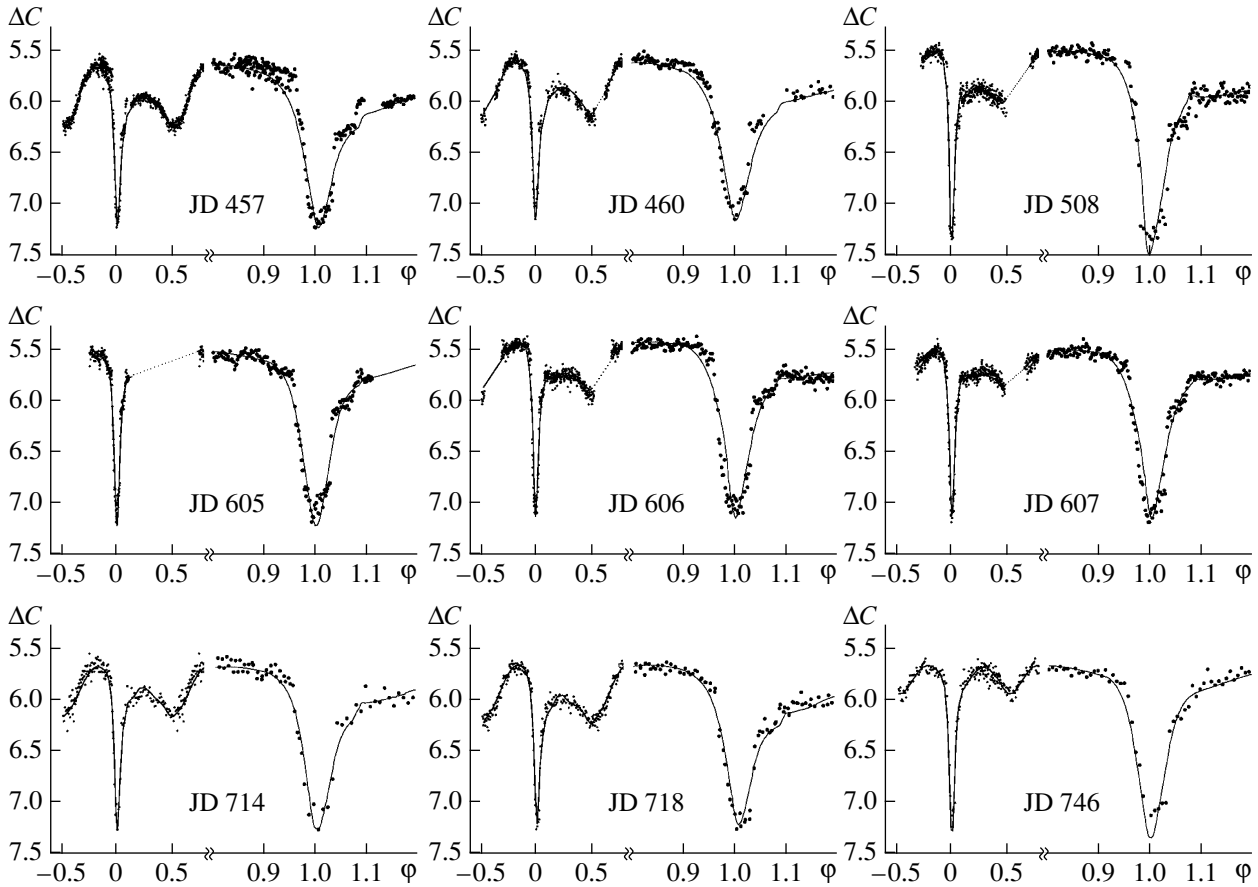

Fig. 8. Unaveraged observed light curves of V1239 Her (dots) obtained in 2013–2014 together with the synthesized theoretical curves corresponding to the parameters from Table 4 (solid curve). In each panel, the left side shows the orbital curve and the right side observations in the region of the primary minimum ($\varphi \sim 0.8$–1.2).

emitted by the leeward side of the hot ellipsoid. As expected, the flux from the hot spot is determined by the product of the spot size ($\sim R_{sp}$) and spot temperature ($\sim T_U$).

4. The hot stream (primarily its base, i.e., regions adjacent to the lateral surface of the disk) contributes to the combined flux in two fragments of the orbital curve, at orbital phases $\varphi \sim 0.2$ and 0.8, due to the appearance of the stream's windward and leeward sides in the line of sight. Table 4 shows that the temperatures in these regions ($\Delta T_{ww,\max}$ and $\Delta T_{lw,\max}$) differ only slightly, by 0.02% to 6%. The visibility of the shocked region is more favorable for the leeward side of the stream compared to the windward side, and the flux from the former region is higher by a factor of 1.5–2.

The presence of flux from the stream around phases $\varphi \sim 0.2$ leads to a slight hump in the light curve at the eclipse egress: in the absence of this contribution, the flux from the system would have been at the level of the minimum at phases $\varphi \sim 0.5$–0.6.

Finally, the light curve for JD 2456746 (and possibly JD 2456605) displays a complete absence of a hot spot. This circumstance leads to a separation of the data points into two arms when plotting the combined light curve with all the observations (see Section 3 and panel *10* in Fig. 2). The temperatures at the base of the hot stream are lowest here, compared to the other light curves; the temperature at the stream axis T_U is below the mean temperature at the outer edge of the disk. This may testify to a decreased rate of matter flow from the red dwarf, a decreased density of the gas stream, and thereby a corresponding decreased intensity of the shock.

Figure 10 presents schematic images of V1239 Her in the plane of the sky, to illustrate the relative sizes of the system components (Fig. 10a) for an inclination $i = 82.64°$ at orbital phase $\varphi = 0.80$ (Fig. 10b). We used the disk parameters derived from the light curve of JD 2456457 to plot this figure.

8. DISCUSSION

The quiescent light curve of V1239 Her displays a narrow primary minimum (to $\sim 1.5^m$ in depth), re-

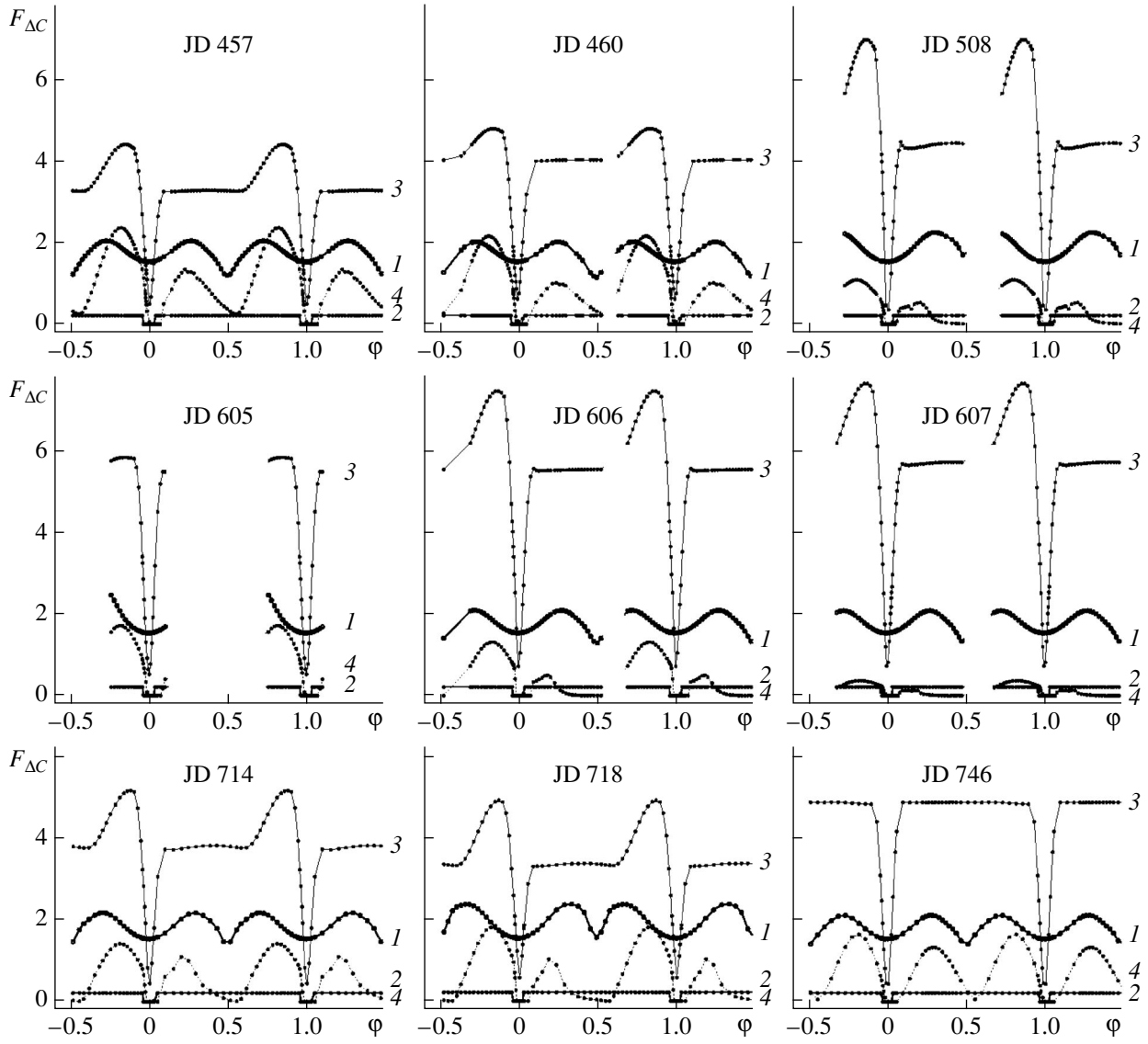

Fig. 9. Contribution of different components of V1239 Her to the combined flux in quiescence in 2013–2014 (in relative units): (*1*) the red dwarf, (*2*) the white dwarf, (*3*) the accretion disk with the hot spot on its lateral surface, and (*4*) the hot stream.

sulting from the eclipse of the WD by the secondary, as well as a partial eclipse of the disk and regions of energy release in the hot stream. Prior to the primary minimum ingress, there is a hump with an integrated-light amplitude up to 0.5^m. The egress from the primary minimum is observed at phases $\varphi \sim 0.12-0.15$, after which the brightness gradually decreases by $\sim 0.2^m$. A secondary eclipse is clearly visible at phase $\varphi \sim 0.5$, after which the brightness increases smoothly until the onset of the hump, $\varphi \sim 0.8$. This physical pattern can be reproduced equally well in a traditional hot-spot model [28] and in the hot-stream and combined models [17–19].

However, the regions of out-of-eclipse brightness display smooth variations, though with a small amplitude. As was noted in Section 6, the combined model is better able to describe the light-curve shape than a model having only a hot spot. Let us consider the behavior of the disk parameters derived in our model.

In quiescence, V1239 Her exhibits fairly active variations of the disk temperature, radius, possibly the viscosity (as indicated by variations of the parameter α_g), and the rate of matter flow (Tables 4, 5). Though we have relatively little data, let us try to follow the time dependences of the different parameters of the disk: its radius R_d/ξ, α_g, the disk temperature in the transition layer $T_{\rm in}$, the thickness of the disk's outer edge β_d, and the angle β_1 between the axis of the gas stream and the line joining the centers of mass of the binary components. The parameter β_1 indirectly describes the velocity of the matter flow

Table 5. Fluxes F from the components of V1239 Her in 2013–2014 in relative units, derived from the solution for the system parameters in the combined model for the nine sets of observations

Parameter	Date, JD 2456000+								
	457	460	508	605	606	607	714	718	746
Red dwarf									
Minimum $\varphi = 0.0$	1.55	1.55	1.55	1.55	1.55	1.55	1.55	1.55	1.55
Minimum $\varphi = 0.5$	1.21	1.19	1.71	–	1.30	<1.34	1.47	1.56	1.42
Quadrature	2.06	2.03	2.26	2.48	2.10	2.10	2.19	2.38*	2.12
White dwarf									
Minimum $\varphi = 0.0$	0.0	0.0	0.0	0.0	0.0	0.0	0.0	0.0	0.0
Maximum	0.22	0.22	0.22	0.22	0.22	0.22	0.22	0.22	0.22
Disk									
Minimum $\varphi = 0.0$	0.50	0.62	0.36	0.53	1.06	0.73	0.45	0.57	0.44
⟨Plateau $\varphi = 0.1–0.6$⟩	3.3	4.0	4.4	>5.5	5.6	5.7	3.8	3.4	4.9
Hump	4.44	4.82	7.02	5.87	7.50	7.68	5.19	4.93	4.9
Hot stream									
Minimum $\varphi = 0.0$	0.0	0.08	0.0	0.0	0.0	0.0	0.0	0.0	0.0
Maximum $\varphi \sim 0.2$	1.36	1.02	0.53	–	0.51	0.14	1.10	1.03	1.34
Maximum $\varphi \sim 0.8$	2.38	2.17	1.09	1.73	1.32	0.37	1.43	1.81	1.65

* The quadratures are displaced to phases $\varphi \sim 0.34$ and ~ 0.66.

from the secondary: the larger this parameter, the lower the velocity in the gas stream.

The corresponding dependences are presented in Fig. 11, and Table 6 summarizes the character of the variations for these parameters. Note that the light curve for the last night of our observations differs qualitatively from the other light curves: it does not show a pre-eclipse hump due to light from the leeward side of the hot stream and from the hot spot. The points corresponding to JD 2456718–746 are joined with dashed lines.

Table 6. Observed time variations of the disk parameters

JD 2456000+	Δt, days	ΔN	R_d/ξ	α_g	$T_{\rm in}$	$0.5\beta_d$	β_1
457–460	3	30	*1*	*2s*	*2s*	*2w*	*1*
460–508	48	478	*2*	*3*	*3*	*3*	*2*
508–605	97	968	*3*	*3w*	*3*	*2*	*3*
605–606	1	10	*1*	*2s*	*2s*	*3s*	*2s*
606–607	1	10	*1*	*1*	*1*	*1*	*2s*
607–714	107	1073	*3w*	*3*	*3*	*3w*	*2w*
714–718	4	40	*3*	*3*	*3*	*3s*	*3s*
718–746	28	280	*2*	*2*	*2*	*2*	*2*

Character of variations: (*1*) no change, (*2*) decrease, (*2w*) weak decrease, (*2s*) strong decrease, (*3*) increase, (*3w*) weak increase, (*3s*) strong increase.

Analysis of Fig. 11 and Table 6 leads to the following conclusions.

1. We can roughly subdivide the intervals between the data sets into three groups: short (10–40 orbital cycles $P_{\rm orb}$), intermediate $(280 - 480)P_{\rm orb}$, and long (more than $960P_{\rm orb}$). Changes during intermediate and long intervals do not provide full information. Changes during short time intervals can provide lower limits for a parameter's variation time.

2. During short time intervals ($<30P_{\rm orb}$), the disk radius R_d was constant within the uncertainties; variations of the disk radius were already insignificant for $\Delta N \sim (30–40)P_{\rm orb}$.

3. Appreciable variations of α_g can occur within times $\sim 10P_{\rm orb}$. The rate of variation of α_g during a single orbital cycle can reach $\Delta\alpha_g/\Delta N \sim 0.015$ (for JD 2456605–606); in other cases, this rate is an order of magnitude lower, or this parameter remains constant within the uncertainties.

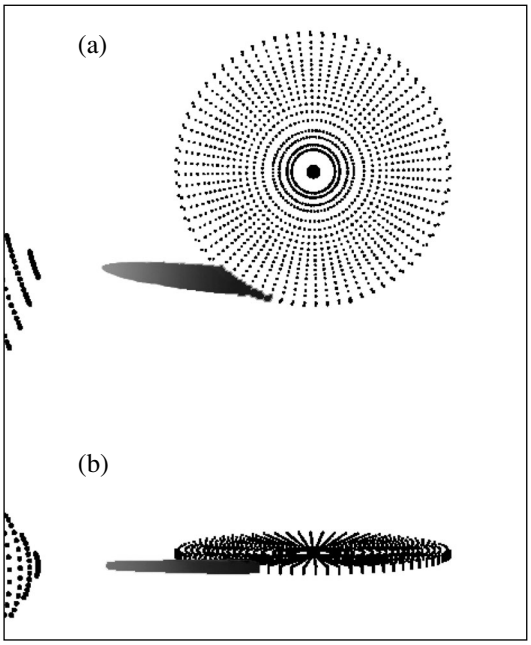

Fig. 10. Schematic images of the V1239 Her system.

4. The thickness of the disk's outer edge, β_d, can also vary within $\sim 10P_{\rm orb}$.

5. Even sharper variations (on time intervals $<10P_{\rm orb}$) are exhibited by the inclination of the gas stream, β_1.

6. Significant sharp changes in α_g, $T_{\rm in}$, and β_d can also occur with the disk radius remaining constant. There is no single relation between the variations of R_d and those of the other parameters, although there is a tendency for sharp decreases of the disk radius to be accompanied by equally sharp increases in the disk thickness at its outer edge; this thickness generally decreases with increasing R_d.

7. During the studied time interval ($\sim 3000P_{\rm orb}$), after its fairly sharp decrease from $R_d \sim 0.48\xi$ to $\sim 0.38\xi$, starting with the 500th cycle, the disk radius exhibits a systematic increase to $\sim 0.56\xi$.

8. The parameter α_g exhibits a systematic increase, i.e., an approach toward its equilibrium state, accompanied by a steep decrease in the viscosity during $\sim 10P_{\rm orb}$, approximately in the middle of our observations ($\sim 1500P_{\rm orb}$), with the disk radius remaining unchanged, after which it continues its smooth increase. The behavior of the temperature in the transition layer, $T_{\rm in}$, generally repeats that of α_g during the entire time covered by our observations.

9. During the sharp decrease in R_d (near JD 508), the thickness of the disk's outer edge reached its maximum during our observations; subsequently, the increase of the disk radius is accompanied by a decrease in the thickness of its outer edge.

10. Prior to JD 2456746, in the data set for JD 718, the radius and viscosity of the disk were the highest during the studied time interval; the temperature in the transition layer was also fairly high, and exceeded the mean temperature of the WD by a factor ~ 2. The thickness of the disk's outer edge also increased to 2.6°, which exceeds its minimum value by a factor of ~ 3. All these findings suggest a considerable accumulation of matter in the body of the disk.

11. The disappearance of the hot spot in the data set for JD 746 was accompanied by an abrupt decrease of all four parameters. The decrease of the temperature in the region of interaction between the gas stream and the disk halo takes place in the presence of a decreased temperature in the transition layer; i.e., under the conditions of a moderate accretion rate, decreased disk radius, and a radial temperature distribution in the disk that is closer to the equilibrium distribution. The thickness of the disk's outer edge is also minimum at this time.

12. Comparing the parameters from the two last data sets (JD 718 and 746), we conclude that there was a significant decrease of the disk mass between them.

13. Finally, let us consider the time behavior of the angle β_1, which provides information about the rate of matter outflow from the inner Lagrange point: an increase of β_1 from $\sim 12°$ to $\sim 26°$ indicates a significant decrease in the gas velocity in the stream. β_1 is largest in the data set for JD 718, indicating a lower rate of matter input from the inner Lagrange point. This also provides evidence for a lower disk mass in the data set for JD 746. This change in β_1, and hence in the initial velocity of the matter outflow from the secondary, could have various origins: changes in the red dwarf's temperature, the turbulence regime, oscillation processes, etc. Unfortunately, the data are insufficient to enable us to draw firm conclusions.

It is usually believed that secondaries of CVs with periods shorter than six hours are ordinary main-sequence red dwarfs. However, several stars that are too hot for their masses have been found recently. A list of such CVs can be found in [29]. Among stars with orbital periods in or close to the period gap, apart from V1239 Her, we should mention QZ Ser ($P_{\rm orb} = 2$ hours), CSS J134052.0+151341 ($P_{\rm orb} = 2.45$ hours), and the new object SDSS J001153.08−064739.2 ($P_{\rm orb} = 2.41$ hours). The red dwarf in the system has a considerably lower mass than follows from its orbital period and is hotter than follows from its mass, as was noted by Littlefair et al. [9], who also noted that the secondary is a quite evolved star, with its mass and effective temperature corresponding to a star that has started matter transfer at an epoch when

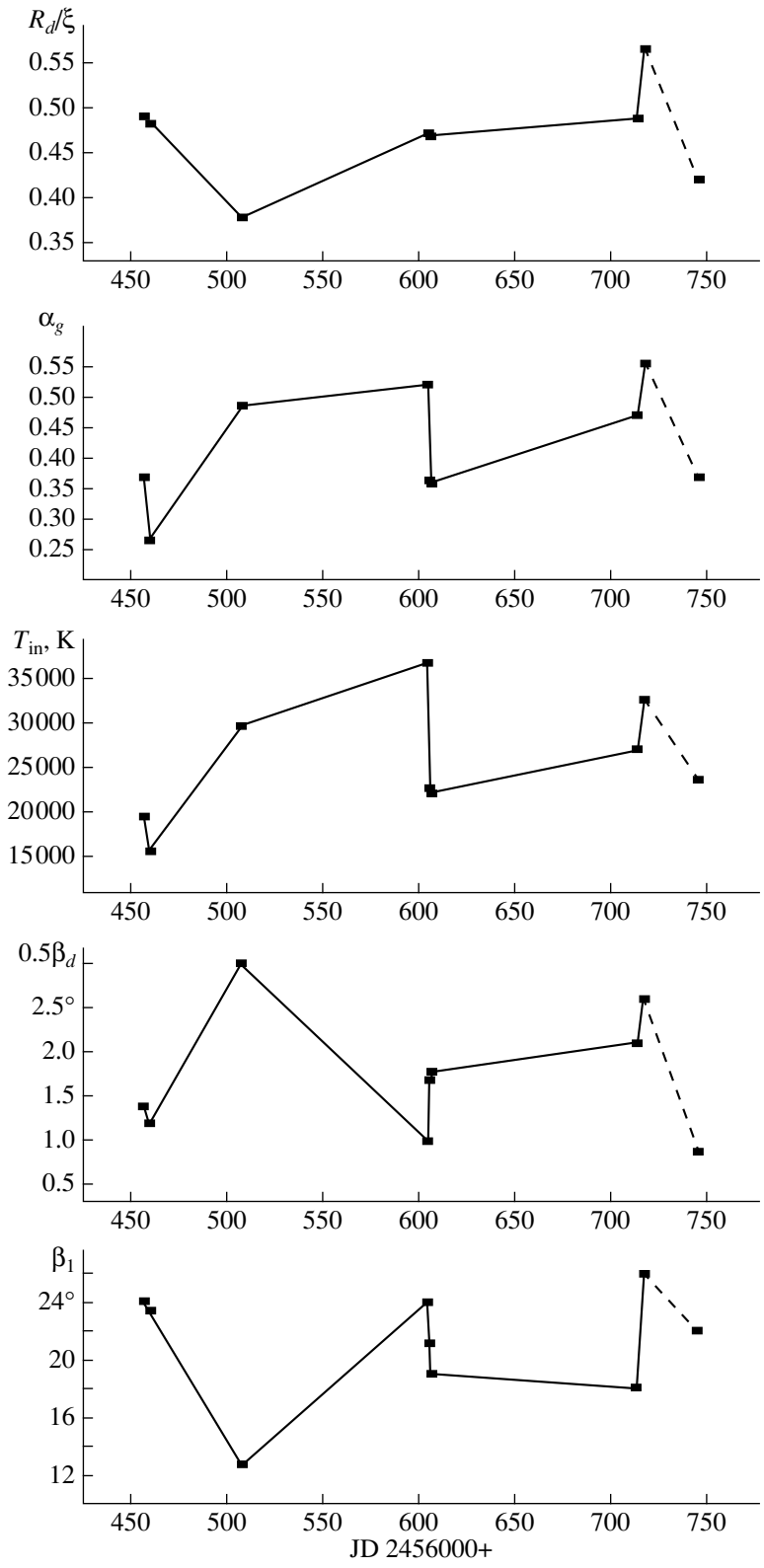

Fig. 11. Time dependences of various disk parameters: the radius R_d/ξ, α_g, disk temperature in the transition layer T_{in}, thickness of the disk's outer edge β_d, and the angle β_1.

the fraction of hydrogen in its center had appreciably decreased.

9. CONCLUSION

1. We have performed photometric monitoring of the eclipsing cataclysmic variable V1239 Her with a time resolution of 15–30 s in white (integrated, unfiltered) light.

2. We have refined the ephemeris of the orbital variations using all available observations (our data and data from the literature).

3. The light curve of V1239 Her in quiescence usually has the shape classical for CVs, with a pre-eclipse hump. However, V1239 Her was repeatedly found in states without the pre-eclipse hump. This follows both from our observations (JD 2456746) and the observations of Boyd et al. [8].

4. We determined the parameters of the accretion disk in quiescence in a combined model taking into account the simultaneous presence of a hot spot and a hot stream in the system. The light curves of V1239 Her obtained during quiescence can be described successfully using this model.

5. We have derived lower limits for the variation times of the disk parameters α_g, $T_{\rm in}$, and β_d, which can change appreciably within less than 10 orbital cycles. The disk radius can remain unchanged within the uncertainties while these parameters are displaying very sharp variations.

6. The light curve for the data set of JD 746 (and possibly, of JD 605) demonstrates a complete absence of a hot spot on the lateral surface of the disk. The spot radius, spot temperature, and the temperature at the base of the hot ellipsoid are the lowest among those derived for the other light curves at these times, and the temperature on the axis of the stream is below the mean temperature at the outer edge of the disk.

7. The time behavior of the angle β_1 provides evidence for a twofold change in the matter velocity in the gas stream during our observations.

8. Considering the disk parameters for the last two data sets (JD 718 and 746), which are separated by 280 orbital cycles, and the significant decrease in the initial velocity of the matter flow from L_1 in the data set for JD 718, we conclude that a considerable decrease in the accretion-disk mass occurred between these two epochs, due to both a reduced outflow rate and a possible infall of a considerable portion of the disk matter on the WD surface. In the latter case, some increase in the flux from the system should have been observed; however, we were not able to find any reliable information on the brightness of V1239 Her in the interval between our data sets for JD 718 and 746.

9. Thus, parameters of the disk, such as its radius, viscosity, temperature, and possibly its density, vary regularly between outbursts in the V1239 Her system. It is not excluded that these variations are due to instability processes in the atmosphere of the evolved secondary.

10. All these processes occur in a system that is located in the period gap, where, according to evolutionary computations, there is no outflow from the secondary, or such outflow is minimal.

11. It is usually believed that the secondaries of CVs with periods shorter than six hours are ordinary main-sequence red dwarfs. However, several stars too hot for their masses have been found recently [29]. Among stars with orbital periods in or close to the period gap, apart from V1239 Her, we should mention QZ Ser ($P_{\rm orb} = 2$ hours), CSS J134052.0+151341 ($P_{\rm orb} = 2.45$ hours), and the new object SDSS J001153.08–064739.2 ($P_{\rm orb} = 2.41$ hours). The fact that the red dwarf in the system is hotter than expected was noted by Littlefair et al. [9], who also noted that the secondary is more evolved than is generally believed.

ACKNOWLEDGMENTS

The authors thank M. Gabdeev (SAO, Russian Academy of Sciences) for the observations with the Zeiss-1000 telescope on August 2, 2013. N.I. Shakura and P.Yu. Golysheva are grateful for supporting the work by the grant of the Russian Science Foundation (project no.14-12-00146).

REFERENCES

1. A. M. Cherepashchuk, N. A. Katysheva, T. S. Khruzina, and S. Yu. Sugarov, *Highly Evolved Close Binary Stars: Catalogue* (Gordon and Breech, Amsterdam, 1996).
2. N. A. Katysheva and E. P. Pavlenko, Astrofizika **46**, 147 (2003).
3. D. Nogami, T. Kato, H. Baba, and S. Matsuda, Publ. Astron. Soc. Jpn. **50**, L1 (1998).
4. E. P. Pavlenko, T. Kato, O. I. Antonyuk, T. Ohshima, F.-J. Hambsch, K. A. Antonyuk, A. A. Sosnovskij, A. V. Baklanov, S. Yu. Shugarov, N. V. Pit, Ch. Nakata, G. Masi, K. Nakajima, H. Maehara, P. A. Dubovsky, I. Kudzej, M. V. Andreev, Y. G. Kuznyetsova, and K. A. Vasiliskov, arXiv:1408.4285 [astro-ph.SR] (2014).
5. Z.-B. Dai and S.-B. Qian, ASP Conf. Ser. **451**, 127 (2011).
6. Z.-B. Dai and S.-B. Qian, Mem. Soc. Astron. Ital. **83**, 614 (2012).

7. P. Szkody, A. Henden, O. Fraser, N. Silvestri, J. Bochanski, M. A. Wolfe, M. Agüeros, B. Warner, P. Woudt, J. Tramposch, L. Homer, G. Schmidt, G. R. Knapp, S. F. Anderson, K. Covey, H. Harris, S. Hawley, D. P. Schneider, W. Voges, and J. Brinkmann, Astron. J. **128**, 1882 (2004).
8. D. Boyd, A. Oksanen, and A. Henden, J. Brit. Astron. Assoc. **116**, 4 (2006).
9. S. P. Littlefair, V. S. Dhillon, T. R. Marsh, and B. T. Gänsicke, Mon. Not. R. Astron. Soc. **371**, 1435 (2006).
10. C. D. J. Savoury, S. P. Littlefair, V. S. Dhillon, T. R. Marsh, B. T. Gänsicke, C. M. Copperwheat, P. Kerry, R. D. G. Hickman, and S. G. Parsons, Mon. Not. R. Astron. Soc. **415**, 2025 (2011).
11. W. H. Press, B. P. Flannery, and S. A. Teukolsky, *Numerical recipes, The Art of Scientific Computing* (Cambridge Univ. Press, Cambridge, 1986).
12. T. Kato, A. Imada, M. Uemura, D. Nogami, H. Maehara, R. Ishioka, H. Baba, K. Matsumoto, H. Iwamatsu, K. Kubota, K. Sugiyasu, Y. Soejima, Y. Moritani, T. Ohshima, H. Ohashi, J. Tanaka, M. Sasada, A. Arai, K. Nakajima, S. Kiyota, K. Tanabe, K. Imamura, N. Kunitomi, K. Kunihiro, H. Taguchi, M. Koizumi, N. Yamada, Y. Nishi, M. Kida, S. Tanaka, R. Ueoka, H. Yasui, K. Maruoka, A. Henden, A. Oksanen, M. Moilanen, P. Tikkanen, M. Aho, B. Monard, H. Itoh, P. A. Dubovsky, I. Kudzej, R. Dancikova, T. Vanmunster, J. Pietz, G. Bolt, D. Boyd, P. Nelson, Th. Krajci, L. M. Cook, K. Torii, D. R. Starkey, J. Shears, L.-T. Jensen, G. Masi, R. Novak, T. Hynek, R. Kocian, L. Kral, H. Kucakova, M. Kolasa, P. Stastny, and B. Staels, Publ. Astron. Soc. Jpn. **61**, S395 (2009).
13. T. Kato, F.-J. Hambsch, H. Maehara, G. Masi, I. Miller, R. Noguchi, Ch. Akasaka, T. Aoki, H. Kobayashi, K. Matsumoto, Sh. Nakagawa, T. Nakazato, T. Nomoto, K. Ogura, R. Ono, K. Taniuchi, W. Stein, A. Henden, E. de Miguel, S. Kiyota, P. A. Dubovsky, I. Kudzej, K. Imamura, H. Akazawa, R. Takagi, Y. Wakabayashi, M. Ogi, K. Tanabe, J. Ulowetz, E. Morelle, R. D. Pickard, T. Ohshima, K. Kasai, E. P. Pavlenko, O. I. Antonyuk, A. V. Baklanov, K. Antonyuk, D. Samsonov, N. Pit, A. Sosnovskij, C. Littlefield, R. Sabo, J. Ruiz, Th. Krajci, Sh. Dvorak, A. Oksanen, K. Hirosawa, W. N. Goff, B. Monard, J. Shears, D. Boyd, I. B. Voloshina, S. Yu. Shugarov, D. Chochol, A. Miyashita, J. Pietz, N. Katysheva, H. Itoh, G. Bolt, M. V. Andreev, N. Parakhin, V. Malanushenko, F. Martinelli, D. Denisenko, Ch. Stockdale, P. Starr, M. Simonsen, P. J. Tristram, A. Fukui, T. Tordai, R. Fidrich, K. B. Paxson, K. Itagaki, Y. Nakashima, S. Yoshida, H. Nishimura, T. V. Kryachko, A. V. Samokhvalov, S. A. Korotkiy, B. L. Satovski, R. Stubbings, G. Poyner, E. Muyllaert, V. Gerke, W. MacDonald II, M. Linnolt, Y. Maeda, and H. Hautecler, Publ. Astron. Soc. Jpn. **65**, 23 (2013).
14. S. P. Littlefair, V. S. Dhillon, T. R. Marsh, B. T. Gänsicke, J. Southworth, I. Baraffe, C. A. Watson, and C. Copperwheat, Mon. Not. R. Astron. Soc. **388**, 1582 (2008).
15. S. P. Littlefair, V. S. Dhillon, T. R. Marsh, B. T. Gänsicke, I. Baraffe, and C. A. Watson, Mon. Not. R. Astron. Soc. **381**, 827 (2007).
16. I. B. Voloshina and T. S. Khruzina, Astron. Rep. **56**, 819 (2012).
17. D. V. Bisikalo, A. A. Boyarchuk, O. A. Kuznetsov, and V. M. Chechetkin, Astron. Rep. **41**, 786 (1997).
18. D. V. Bisikalo, A. A. Boyarchuk, O. A. Kuznetsov, T. S. Khruzina, A. M. Cherepashchuk, and V. M. Chechetkin, Astron. Rep. **42**, 33 (1998).
19. D. V. Bisikalo, A. A. Boyarchuk, V. M. Chechetkin, and D. Molteni, Mon. Not. R. Astron. Soc. **390**, 39 (1998).
20. D. V. Bisikalo, A. A. Boyarchuk, P. V. Kaigorodov, and O. A. Kuznetsov, Astron. Rep. **47**, 809 (2003).
21. M. Makita, K. Miyawaki, and T. Matsuda, Mon. Not. R. Astron. Soc. **316**, 906 (2000).
22. K. Sawada and T. Matsuda, Mon. Not. R. Astron. Soc. **255**, 17P (1992).
23. Z. Kopal, *Close Binary Systems* (Chapman and Hall, London, 1959).
24. T. S. Khruzina, Astron. Rep. **88**, 426 (2011).
25. T. S. Khruzina, Astron. Rep. **44**, 446 (2000).
26. N. I. Shakura and R. A. Sunyaev, Astron. Astrophys. **24**, 337 (1973).
27. D. Himmelblau, *Applied Nonlinear Programming* (McGraw-Hill, New York, 1972; Mir, Moscow, 1975), p. 163.
28. B. Warner, *Cataclysmic Variables* (Cambridge Univ. Press, Cambridge, 1995).
29. A. Rebassa-Mansergas, S. G. Parsons, C. M. Copperwheat, S. Justham, B. T. Gänsicke, M. R. Schreiber, T. R. Marsh, and V. S. Dhillon, Astrophys. J. **790**, 28 (2014).

Translated by N. Samus'